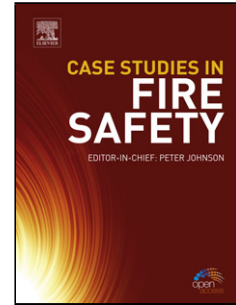# Accepted Manuscript

Title: High-throughput characterization of the effects of H_2O vapour on early oxidation across $Al_xFe_yNi_{1−x−y}$ composition space

Author: Matthew A. Payne James B. Miller Andrew J. Gellman

Please cite this article as: {http://dx.doi.org/

High-throughput characterization of the effects of H_2O vapour on early oxidation across $Al_xFe_yNi_{1-x-y}$ composition space

Matthew A. Payne [a, b], James B. Miller [a, b], Andrew J. Gellman [a, b]

[a] Department of Chemical Engineering, Carnegie Mellon University, Pittsburgh, PA 15213 (USA)
[b] DOE - National Energy Technology Laboratory, P.O. Box 10940, Pittsburgh, PA 15236 (USA)

Corresponding author:
Andrew J. Gellman
Carnegie Mellon University
Department of Chemical Engineering
5000 Forbes Avenue
Pittsburgh, PA 15213 (USA)
+1 (412) 268-3848
gellman@cmu.edu

Highlights

- $Al_xFe_yNi_{1-x-y}$ ($x = 0 \rightarrow 1$, $y = 0 \rightarrow 1-x$) oxidation in H_2O/air at 427 °C was studied.

- The continuous composition boundary of internal/external oxidation was identified.

- Data were compared with $Al_xFe_yNi_{1-x-y}$ oxidation in dry air at 427 °C.

- The differences are assessed in terms of a modified Wagner-Maak criterion.

ABSTRACT

The presence of H_2O vapour in an oxidizing environment can increase the critical aluminium concentration, N_{Al}^*, required to establish a passivating Al_2O_3 scale in multicomponent alumina-forming alloys. This work used $Al_xFe_yNi_{1-x-y}$ composition spread alloy film combinatorial libraries to determine $N_{Al}^*(x, y)$ continuously across $Al_xFe_yNi_{1-x-y}$ composition space ($x = 0 \rightarrow 1$, $y = 0 \rightarrow [1-x]$) in a 10% H_2O/air mixture at 427 °C. The $N_{Al}^*(x, y)$ in this environment was significantly higher across much of composition space than that previously measured in dry air. Physical insights from the observed differences are considered using a modified Wagner-Maak model.

KEYWORDS

A. aluminium; A. iron; A. nickel; B. Raman spectroscopy; B. XPS; C. oxidation

1. INTRODUCTION

1.1. N_{Al}^* in AlFeNi-based alumina formers

The $Al_xFe_yNi_{1-x-y}$ (subscripts designate atomic fractions) system serves as an ideal model of a ternary "alumina former", a term that refers generically to any of a class of alloys that achieve high-temperature oxidation resistance under thermochemically harsh operating conditions due to the preferential formation of a passivating alumina (Al_2O_3) scale at or near their surface [1–5]. Alumina formers are much more corrosion resistant in the presence of H_2O vapour than similar materials which form SiO_2 or Cr_2O_3 scales, and thus are preferable for use in a number of industrially important environments [6,7]. The Al content of an alloy must meet or exceed some "critical Al concentration", N_{Al}^*, for an Al_2O_3 scale to be established, a behaviour termed "external oxidation" [4–6,8–14]. Subcritical Al concentrations result instead in "internal oxidation", i.e. the ongoing formation of discontinuous Al_2O_3 precipitates in the alloy bulk [5,6,8–12]. Fe and Ni are two major components included in alumina-forming austenitic stainless steels, alloys designed for applications that require both oxidation resistance and structural integrity [5,15–17]. In these and similar alloys where both oxidation resistance and mechanical properties are important, it is desirable for the Al content to exceed N_{Al}^* by as little as possible, as excess Al tends to increase brittleness [6,9,13,15,18,19]. A significant challenge in the design of such materials is that the value of N_{Al}^* is highly system-dependent, and may vary as a function of both alloy composition and the chemical nature of the oxidizing environment [6,7]. An example of particular practical importance is that that the presence of H_2O vapour is frequently found to be detrimental to the oxidation resistance of scale-forming alloys [5,12,16,20–22]. In both Fe- and Ni-containing alumina formers, it has been directly observed that N_{Al}^* is higher in the presence of H_2O vapour than in dry environments, but the physical origin of this phenomenon has yet to be definitively determined [5,12,16,20,22]. Developing an improved understanding of the effects of H_2O vapour in the oxidizing environment is critically important to the rational design of next-generation alumina formers.

1.2. High-throughput study of oxidation across $Al_xFe_yNi_{1-x-y}$ composition space

We have previously reported a high-throughput methodology for assessing oxidation behaviour at all possible compositions of a given ternary alloy [23]. This was accomplished using $Al_xFe_yNi_{1-x-y}$ composition spread alloy films (CSAFs), combinatorial sample libraries containing lateral composition gradients, as shown schematically in Figure 1. Oxidation of $Al_xFe_yNi_{1-x-y}$ CSAFs was analysed using various spatially resolved techniques, including energy-dispersive X-ray spectroscopy (EDX), Raman spectroscopy, and X-ray photoelectron spectroscopy (XPS). The results of these analyses allowed us to characterize phenomenologically the oxidation behaviour occurring across all of $Al_xFe_yNi_{1-x-y}$ composition space in dry air at 427 °C and to identify the continuous $N_{Al}^*(x, y)$ boundary defining the minimum Al content for which a passivating Al_2O_3 scale was established. The goals of the work reported herein were to apply the same high-throughput methodology to study the oxidation of $Al_xFe_yNi_{1-x-y}$ in a mixture of air and H_2O vapour at 427 °C, to identify any observable effects of H_2O vapour on the oxidation behaviour or on $N_{Al}^*(x, y)$, and finally, to consider the physical origins of any observed differences. The 427 °C oxidation temperature used for our high-throughput studies was chosen based on experimental constraints, but it should be noted that operating temperatures of practical interest for alumina-forming alloys are more typically between ~600-1200 °C [4,12,15,18]. Thus, it is important to keep in mind that the oxidation events occurring in these studies would be considered early/transient in the higher temperature environments generally considered for these types of alloys. The primary intent of the work is to demonstrate the potential value of high-throughput methods as a tool for screening environmental effects on alloy oxidation; to this end, $Al_xFe_yNi_{1-x-y}$ at 427 °C is used as a model system. Potential insights that such "early oxidation" of $Al_xFe_yNi_{1-x-y}$ CSAFs might offer into the oxidation of bulk alloys at higher temperatures will be discussed later.

2. EXPERIMENTAL METHOD

2.1. Preparation of Al$_x$Fe$_y$Ni$_{1-x-y}$ CSAFs

We have developed the ability to prepare full-range ternary CSAFs using a rotatable shadow mask (RSM) CSAF deposition tool, which is described in detail elsewhere [24]. The CSAF layer is physically vapour deposited onto a substrate by e-beam evaporation in the ultra-high vacuum (UHV) environment of the RSM-CSAF deposition tool. Ternary CSAFs are deposited using three confocal e-beam evaporators attached to the tool, one for each elemental component. Partial, line-of-sight shadowing by rotationally adjustable masks mounted between each evaporator and the substrate is used to obtain a gradient in the evaporative flux of each element across the substrate surface. The three elemental gradients decrease linearly from a maximum value to zero in directions controlled by the orientations of their respective masks. Appropriate alignment and mask orientations were previously determined such that the RSM-CSAF deposition tool can be used to create Al$_x$Fe$_y$Ni$_{1-x-y}$ CSAFs with composition gradients that are very close to the ideal, triangular geometry shown schematically in Figure 1. The CSAFs are grown by simultaneous evaporation of the three metal components.

Two Al$_x$Fe$_y$Ni$_{1-x-y}$ CSAFs were prepared for the studies described herein. The preparation methodology is described in detail in our previously published study [23]. The CSAFs were each deposited on the 14×14 mm^2 face of a 2.5 mm-thick polycrystalline-Mo substrate polished to a root mean squared roughness <1.5 nm. The substrate was sputtered under UHV conditions (~ 10^{-7} Pa base pressure) with a defocused 2 kV Ar$^+$ beam, annealed at 477 °C for 1 h, and then allowed to cool to room temperature. The Ar$^+$ sputtering was repeated immediately before deposition of the Al$_x$Fe$_y$Ni$_{1-x-y}$ CSAF. Al, Fe, or Ni pieces of ≥99.98% purity were used as source materials in the e-beam evaporators. A quartz crystal microbalance (QCM) was used to monitor deposition rates and determine the power setting required for each evaporator to achieve a target flux for its respective metal. The targeted deposition rates were chosen to yield an Al$_x$Fe$_y$Ni$_{1-x-y}$ CSAF thickness of ~120 nm while the three metals were co-deposited for 500 min (due to limitations of the e-beam evaporators, this is near the maximum thickness that is reasonably achievable). Immediately upon conclusion of a

deposition, the CSAF was annealed to 427 °C for 2 h and then cooled to room temperature in UHV. We have previously performed XPS depth profiling which shows that this preparation results in a homogeneous distribution of Al, Fe, and Ni across the CSAF cross section, with no significant concentration of contaminants detected within the film. Each CSAF remained under UHV until the chamber was vented, at which point it was exposed to ambient air for a period of ~15 min while it was transferred to a *Tescan* Vega3 scanning electron microscope (SEM) operated at ~10^{-2} Pa.

2.2. Spatial mapping of CSAF composition distribution

After deposition, EDX spectra obtained in the SEM were used to map $Al_xFe_yNi_{1-x-y}$ composition as a function of position on each CSAF. The experimental procedure for doing so was developed in our previously published study [23]. EDX measurements of $Al_xFe_yNi_{1-x-y}$ composition were taken at discrete locations across the 12×12 mm^2 region in the centre of the 14×14 mm^2 CSAF surface. The measurements were spaced by 1 mm on a 13×13 square grid. The EDX spectra (0-10 keV, 10 eV binning, >300,000 total counts per spectrum) were collected from 50×50 µm^2 area scans with the SEM beam operating at 11.24 kV. The $Al_xFe_yNi_{1-x-y}$ composition of the CSAF was determined from each spectrum by quantification using the *Oxford Instruments* software package INCA ThinFilmID, which was used to account for the compositional inhomogeneity with depth in the beam interaction volume. The assumption used for processing the spectra was that the $Al_xFe_yNi_{1-x-y}$ was present as a flat, homogenous layer on the Mo substrate, which we have previously confirmed to be reasonably accurate via XPS depth profiling. The EDX measurements of CSAF composition were repeated three times at each grid location, and the results were averaged to reduce noise.

The 13×13 grid of EDX composition measurements was used to determine a least-squares fit to a unique composition distribution model (CDM) for each CSAF. The CDM describes the $Al_xFe_yNi_{1-x-y}$ composition of the CSAF continuously as a function of real-space position on the surface. It is defined using 12 parameters describing the flux gradients of the metal components deposited with the RSM-CSAF deposition tool [24]. The CDM assumptions, as well as its functional form, are described in the appendix of our previous study [23]. The purpose of the CDM is twofold: first, to allow accurate

interpolation of CSAF composition at real-space locations that were not explicitly measured with EDX and, second, to allow accurate estimation of the real-space location on the surface where any specific $Al_xFe_yNi_{1-x-y}$ composition of interest can be found.

2.3. Oxidation and visual analysis of CSAFs

The $Al_xFe_yNi_{1-x-y}$ CSAFs were oxidized at an elevated temperature in a ceramic boat in the centre of a quartz tube furnace (~60 cm long, 2 cm diameter) with one end open to atmosphere and the other end connected to a gas-introduction manifold. A regulator was used to maintain a continuous flow of ~1 slpm from a cylinder of lab-grade dry air, which was bubbled through a series of two ~1 L heated H_2O baths before being introduced into the furnace tube via the manifold. The H_2O temperature in the first bath in the series was maintained at 61±1 °C, while the second was maintained at 46±1 °C. The gas-flow lines between the first and second baths and between the second bath and the entrance to the furnace were heated and maintained at >61 °C. The air was introduced near the bottom of each bath through a microporous, stainless-steel fitting which broke the air stream into small bubbles. As a result of humidification in the baths, we estimate that the gas entering the furnace contained an H_2O partial pressure of ~10^4 Pa, the equilibrium vapour pressure at 46 °C. Thus, the gas feed to the furnace was ~10% H_2O in air by volume. Henceforth in this text, this gas feed will simply be referred to as "humid air". Prior to oxidation of an $Al_xFe_yNi_{1-x-y}$ CSAF, the furnace and ceramic boat were preheated until the temperature was stable at 427±1 °C while the humid air was flowing. The boat was then pulled to the open end of the furnace, the CSAF was quickly loaded such that only the underside of the Mo substrate was in direct contact with the ceramic, and the boat/CSAF were pushed back to the centre of the furnace. In three cycles, after total exposure times to the furnace environment, t_{ox}, of 1, 2, and 4 h, the CSAF was removed from the furnace and the bottom of the Mo substrate was placed in contact with aluminium foil to quickly dissipate heat, cooling the sample to near room temperature in ~2 min. On each such occasion, the CSAF was photographed and then loaded into the SEM for further characterization.

Oxidation of $Al_xFe_yNi_{1-x-y}$ CSAFs at 427 °C causes visually observable changes in their surface colouration which can vary markedly with composition, i.e. with real-space

location on the surface. Sharp transitions in surface colouration can sometimes be shown to correlate to a measurable transition in the oxidation behaviour that has occurred in two neighbouring regions of $Al_xFe_yNi_{1-x-y}$ composition space, as described in our previous study of $Al_xFe_yNi_{1-x-y}$ CSAF oxidation in dry air at 427 °C [23]. Photographs of the CSAFs after each oxidation stage allow such visually distinguishable regions to be accurately defined in real space, which is useful in determining locations on the CSAF on which to focus more time-intensive spectroscopic techniques used to characterize oxidation behaviour. Any such data collected in real space can also be rapidly translated into $Al_xFe_yNi_{1-x-y}$ composition space by applying the CDM for the CSAF.

2.4. EDX, Raman, and XPS characterization of CSAF oxidation behaviour

In our previous study, we developed a methodology for the high-throughput characterization of oxidation behaviour across CSAFs using a combination of EDX, Raman spectroscopy, and XPS depth profiling [23]. The same techniques were applied in this work, but were used to characterize the oxidation of $Al_xFe_yNi_{1-x-y}$ CSAFs exposed to humid air instead of dry air at 427 °C. With a few minor exceptions (which will be explicitly stated), the experimental procedures for the various spectroscopic measurements made in this work were identical to those used in our previous study [23].

EDX was used to monitor oxygen uptake at a large number of locations (261 on one sample and 335 on the other) across the CSAFs as a function of t_{ox} (total exposure time to humid air at 427 °C in the furnace). The real-space coordinates of these locations were chosen (with guidance from the CDM fit to each CSAF) such that a high-density sampling of $Al_xFe_yNi_{1-x-y}$ composition space was obtained from each sample. The precise $Al_xFe_yNi_{1-x-y}$ film composition at each location was first measured by EDX procedures identical to those used in the initial mapping of the composition gradients on the samples. Measurements of the total oxygen content at each location (i.e. the total amount of oxygen present in the entire CSAF cross section), $C_O(x, y)$, were then obtained from additional EDX scans after each $t_{ox} = 0, 1, 2,$ and 4 h. These scans were used to collect spectra (0-10 keV, 10 eV binning, >250,000 total counts per spectrum)

across 50×50 μm^2 areas with the SEM beam operating at 30 kV, for which the C_O of the CSAF is approximately proportional to the oxygen EDX signal scaled by the (much larger) Mo signal from the substrate. For this proportionality approximation to be accurate, the depth sensitivity of EDX must significantly exceed the thickness of the CSAF, which was demonstrated to be the case for EDX measurements made with the SEM beam operating at 20 kV in our previous study [23]. In the present study, EDX measurements of C_O were made using a beam voltage of 30 kV (the maximum possible for our instrument) instead of 20 kV. This was done to further increase the EDX depth sensitivity and, therefore, the accuracy of the proportionality approximation; however, from a practical standpoint, we have not observed any significant difference between using 30 kV and 20 kV spectra to determine C_O when the results are compared on a normalized scale. The EDX measurements of C_O were repeated three times at each location for each sampled t_{ox}, and the results were averaged to reduce noise.

Raman spectroscopy was used to analyse one of the $Al_xFe_yNi_{1-x-y}$ CSAFs after $t_{ox} = 4$ h. A green laser (532 nm wavelength, 200 mW, 100 μm aperture with 50× focusing lens resulting in ~30 μm spot size) was used for excitation, and the Raman-shift spectrum in the range 100-1500 cm^{-1} was measured at 69 locations across the surface using a CCD detector calibrated with Si. The collected spectra were de-spiked using NGSLabSpec software. To focus on transitions between visually distinct regions, the locations for obtaining Raman spectra were chosen in real space based on the appearance of the oxidized surface. Spectra characteristic of an α-Fe_2O_3 and/or $NiFe_2O_4$ phase were observed in some regions, while the spectra in other regions did not reveal any significant Raman scattering.

XPS depth profiling was used to characterize 12 spatially resolved locations on one of the oxidized $Al_xFe_yNi_{1-x-y}$ CSAFs after $t_{ox} = 4$ h. A set of XPS measurements (Al $K\alpha$ X-rays, ~200 μm measurement spot size, hemispherical energy analyser) followed by uniform etching of the analysis area with a rastered Ar^+ beam (3 kV, 1 μA) was performed in 65 identical cycles at each of the locations. For each set of XPS measurements, four different spectra were acquired across 10-14 eV binding-energy ranges containing the non-overlapping Al 2s, Fe 2p$_{1/2}$, Ni 2p$_{3/2}$, and Mo 3p$_{3/2}$ peaks. The spectra were measured using a 0.05 eV step size and 0.2 s dwell time, with a detector

pass energy of 100 eV. The spectral data were quantified by peak fitting with *Thermo* Avantage processing software using the *Thermo* "Smart" background subtraction. The results were used to construct a cross-sectional profile of elemental composition at each location with additional designation of the fraction of each species in an oxidized (as opposed to metallic) chemical state. The XPS peak-fitting procedure was slightly more sophisticated than that used in our previous study. Geometric parameters defining a unique shape for the metallic Al, Fe, Ni, and Mo peaks were determined from measurements made on pure standards that were Ar^+ sputtered with the same settings used for the depth profiling. Under these conditions, the peaks for metallic Al, Fe, and Ni were found to exhibit slight tailing at high binding energies which is captured by the peak-fitting parameters. Oxidation of the metal species in the CSAFs was found to increase the binding energy of the monitored peaks by ~2-5 eV. Geometric fitting parameters were determined for oxidized Al, Fe, Ni, and Mo peaks such that, after fitting, the sum of the metallic and oxidized peaks reasonably reflected the measured spectra for all cycles and locations. This was accomplished by defining a single oxidized peak for Al, Fe, and Mo, but two oxidized peaks were required for Ni. Assignment of the oxidized peaks to specific oxidation states was not attempted. The specific peak-fitting constraints used in the *Thermo* Avantage software and examples of fit spectra are provided in Appendix A. The overall elemental composition at each location/cycle was calculated by normalizing the total peak area for each species by Wagner sensitivity factors. The oxidized-to-metallic ratio for each element was estimated to be equal to the ratio of the area of the oxidized peak(s) to the area of the metallic peak.

3. RESULTS

3.1. Spatial maps of $Al_xFe_yNi_{1-x-y}$ composition gradients from EDX

$Al_xFe_yNi_{1-x-y}$ composition was measured using EDX at discrete points on a 13×13 grid covering the 12×12 mm^2 region in the centre of each of the two CSAFs. Figure 2 shows real-space contour plots of the relative composition of Al, Fe, and Ni in one of the two CSAFs which were mapped using these measurements. The 169 discrete $Al_xFe_yNi_{1-x-y}$ compositions that were measured are plotted as points in the ternary composition

diagram of Figure 2. Because the composition gradients in the CSAF are continuous, all possible compositions within the range of the discretely plotted points on this diagram are also present within the 12×12 mm^2 region. A similar composition map was measured for the other CSAF used in this study. Both CSAFs spanned the full Al$_x$Fe$_y$Ni$_{1-x-y}$ composition space within the 14×14 mm^2 bounds of the surface. The measurement error of the compositions plotted in Figure 2 is about ±0.5 at.%. Additional discussion regarding the accuracy of EDX as a technique for measuring CSAF composition was included in our previous study [23].

3.2. Visual identification of Al$_x$Fe$_y$Ni$_{1-x-y}$ oxidation behaviour boundaries

Distinct changes in the surface colouration of Al$_x$Fe$_y$Ni$_{1-x-y}$ CSAFs occur during oxidation. Figure 3(a, b) shows the images of one of the CSAFs taken at $t_{ox} = 0$ and after $t_{ox} = 4$ h in humid air at 427 °C. The approximate location of the pure-component corners and triangular ternary-composition area (determined using the CDM fit to the CSAF) are overlaid on the images for reference. The most significant changes in surface colouration tend to occur on portions of the CSAF with low Al content, while little change is observable across much of the region of the CSAF with high Al content. The visual appearance of the CSAF at $t_{ox} = 4$ h, shown in Figure 3(b), was largely established by $t_{ox} = 1$ h. The only notable change from 1 to 2 h and 2 to 4 h was a gradual darkening of the brown area surrounding the pure-Ni corner of the ternary-composition area.

A number of boundaries between distinctly coloured regions can be readily observed on the oxidized Al$_x$Fe$_y$Ni$_{1-x-y}$ CSAF in Figure 3(b). Simple visual inspection of the sample can be used to determine the real-space trajectory of any such boundaries, which can then be translated into Al$_x$Fe$_y$Ni$_{1-x-y}$ composition space using the CDM. Three boundaries are identified and marked on the CSAF in Figure 3(b). These boundaries subdivide the triangular ternary-composition area into four increasingly discoloured regions, labelled 1-4. Figure 3(c) shows an image of the other Al$_x$Fe$_y$Ni$_{1-x-y}$ CSAF used in this study after $t_{ox} = 4$ h. The discolouration patterns that were developed on the surfaces of the two CSAFs are quite similar. Equivalent boundaries to those marked on the CSAF in Figure 3(b) were identified and are shown on the second CSAF in Figure

3(c). On each CSAF, the boundaries separating regions 2, 3, and 4 were identified purely on the basis of visual analysis, but the boundary between regions 1 and 2 was identified with partial guidance from SEM imaging. Figure 3(d) shows a low-magnification SEM image (secondary-electron detection) of a large portion of the surface of the CSAF shown in Figure 3(c). The boundary between region 1 (which is not discoloured as a result of oxidation) and region 2 (which is lightly discoloured as a result of oxidation), while fairly obvious near the AlFe binary region of the CSAF, becomes difficult to distinguish visually near the AlNi binary region of the CSAF. However, the transition from region 1 to 2 exhibits clear contrast in the SEM image across the entire CSAF. SEM imaging was used to ensure that the boundary between regions 1 and 2 was identified correctly near the AlNi binary region of the CSAFs.

Figure 3(e) shows a superimposition of the results of the visual analyses from Figures 3(b) and 3(c) upon conversion of the real-space boundaries to composition space using the respective CDM for each CSAF. As discussed in our previous work, the CDM accurately predicts CSAF composition (as would be measured with EDX) at interpolated real-space locations to about ±2 at.% for each alloy component [23]. Thus, Figure 3(e) demonstrates that the results of the visual analyses from the two samples were reproduced to within the expected error of the technique. Figure 3(f) shows an average of the two sets of boundaries in Figure 3(e). These will be used as the basis for subsequent discussion of the spectroscopic analyses used to characterize the oxidation behaviour of $Al_xFe_yNi_{1-x-y}$ in different regions of composition space.

3.3. EDX-monitored oxygen uptake across $Al_xFe_yNi_{1-x-y}$ composition space

EDX was used to make high-throughput measurements of total, relative oxygen content at discrete $Al_xFe_yNi_{1-x-y}$ compositions across each CSAF after $t_{ox} = 0, 1, 2$, and 4 h total oxidation time in humid air at 427 °C. This was done at a large number of points to provide a dense sampling of ternary space; however, the Al-rich ($x > 0.85$) regions of the CSAF were excluded because SEM imaging revealed that these portions of the film were dewetted from the substrate during the initial UHV annealing. Figure 4 shows the oxygen content (C_O) and change in oxygen content (ΔC_O) after $t_{ox} = 0, 1$, and 4 h as measured on the CSAF shown in Figure 3(c). The data from $t_{ox} = 2$ h was not

included because oxygen uptake from 1 to 4 h was very slow. C_O was calculated as the ratio of the O-to-Mo EDX signals and is plotted on an arbitrary, linear scale from 0 to the maximum value measured on either CSAF. The three composition maps on the left display the total C_O measured across the CSAF after $t_{ox} = 0$, 1, and 4 h. The two maps in the centre show ΔC_O during the intervals from 0 to 1 h and from 1 to 4 h. The map on the right shows the ΔC_O data from $t_{ox} = 1$ to 4 h with the scale amplified by a factor of 4.5× to accentuate the important features. The visually determined boundaries from Figure 3(f) are plotted on each of the maps. The data in Figure 4 reveal several important correlations between trends in oxygen uptake and the visually distinct regions 1-4. Small values of C_O were measured across $Al_xFe_yNi_{1-x-y}$ composition space at $t_{ox} = 0$ h (after exposure of the sample to ambient air at room temperature for ~15 minutes), which reach a maximum at $N_{Al} \cong 0.60$. From $t_{ox} = 0$ to 1 h, the ΔC_O plot shows that measurable oxygen uptake occurred across all of composition space except in region 1, but the uptake in region 4 was much larger than in either region 2 or 3. Oxygen uptake from $t_{ox} = 1$ to 4 h is only detectable in region 4. The total C_O after $t_{ox} = 4$ h is slightly higher in regions 2 and 3 than in region 1, but clearly is significantly higher in region 4 than in any of the other three regions.

Additional information regarding the measurement-to-measurement variability when using EDX to determine C_O was provided in our previous work [23]. The measurement precision for the C_O values plotted in Figure 4 is about ±4%. We have also found oxygen uptake data collected from CSAFs using EDX to be very reproducible between samples. Figure 5 shows a comparison of the $C_O(t_{ox} = 4$ h$)$ from Figure 4 with that measured from the other CSAF shown in Figure 3(b). A unique set of $Al_xFe_yNi_{1-x-y}$ compositions was sampled on each CSAF but, due to the high-density coverage of ternary space, it is clear that the maps are very similar.

3.4. Raman identification of oxide phases across $Al_xFe_yNi_{1-x-y}$ composition space

Raman spectra were acquired at 69 locations across the CSAF imaged in Figure 3(c) ($t_{ox} = 4$ h). The locations were chosen to emphasize the transitions between the visually distinct regions 1-4. At each location, one of four characteristic Raman spectra was observed, consistent with either 1) $NiFe_2O_4$ spinel, 2) α-Fe_2O_3, 3) both $NiFe_2O_4$

spinel and α-Fe_2O_3, or else 4) showing no observable Raman scattering activity; representative examples of each of these four types of spectra are shown in Figure 6(left). Figure 6(right) shows the points in $Al_xFe_yNi_{1-x-y}$ composition space at which the different types of spectra were obtained. Phase assignments were made by qualitative comparison to known Raman peak locations for various Al, Fe, and Ni oxide phases. More detailed discussion of the phases considered and a table of their expected Raman peak locations determined from the literature may be found in our previous work [23]. The expected peak positions for $NiFe_2O_4$ and/or α-Fe_2O_3 were sufficient to assign all observable peaks in 63 of the 69 spectra. The remaining 6 spectra, which are marked with an asterisk in Figure 6, contained (either additionally or exclusively) low-intensity peaks that could not be assigned to either $NiFe_2O_4$ or α-Fe_2O_3. The 5 marked points along the FeNi binary contained a weak set of peaks with a primary feature at ~202 cm^{-1} that may be attributable to a MoO_2 phase [25], while the single marked point near the pure-Fe corner contained a weak doublet peak at ~929/937 cm^{-1} which may be indicative of β-$FeMoO_4$ [26]. Such species might have been formed by oxidation of the Mo substrate, but as these points were all located far from the transitions between the numbered regions (and at very low or zero Al content), the details of their origin were not considered further. Figure 6 shows that there are evident correlations between the visually distinct regions 1-4 and the results of the Raman analysis. No significant Raman scattering was observed across the majority of regions 1 and 2. Spectra characteristic of α-Fe_2O_3 were observed exclusively across region 3. In region 4, a transition from spectra characteristic of α-Fe_2O_3, to spectra characteristic of $NiFe_2O_4$, to spectra exhibiting minimal Raman scattering is observed as the Ni-to-Fe ratio increases. It is important to keep in mind that while Raman spectroscopy can allow identification of specific oxide phases at different locations across the CSAF, it does not exclude the possibility of oxides which are not detectable using Raman. Based on the results of our previous study [23], it is expected that Raman-inactive (γ- or amorphous) Al_2O_3 and/or trace amounts of Fe or Ni oxides were formed at all compositions for which no Raman peaks were observed.

3.5. XPS depth profiling of $Al_xFe_yNi_{1-x-y}$ CSAF cross sections

XPS depth profiling was used to measure cross-sectional profiles of elemental composition and chemical state at 12 locations across the CSAF imaged in Figure 3(c). The locations were chosen to sample both binary and ternary compositions on the CSAF in each of the visually distinct regions 1-4. Figure 7 shows the 12 real-space locations that were analysed and the resulting depth profiles obtained at 9 of these locations. The locations are shown on both a photograph of the CSAF (upper left) and a low-magnification SEM image of a portion of the surface (upper right); in both cases the location of the triangular ternary-composition area and the boundaries separating regions 1-4 are shown for reference. The x-axes of the profiles show the total Ar^+ etch time prior to each set of XPS measurements, which were used to determine the relative atomic concentrations shown on the y-axes. While increasing Ar^+ etch time (which is explicitly measured) correlates with increasing sampling depth into the CSAF, it should be noted that this relationship is not expected to be directly proportional for an inhomogeneous cross section due to potentially different etch rates of the various metal and oxide species. Keeping this limitation in mind, the time at which the Mo signal begins to appear can be used to establish an approximate length scale for the x-axis, as shown on the plot in Figure 7(b), since the initial film thickness is roughly known based on the QCM calibrations performed prior to the CSAF deposition. The XPS signal from the Mo substrate had appeared and was increasing with each additional Ar^+ etch cycle near the end of all but one of the depth profiles shown in Figure 7(a-i), indicating that the $Al_xFe_yNi_{1-x-y}$ CSAF was almost completely sputtered away at these locations and, therefore, that the profiles are representative of almost the entire CSAF cross section. XPS depth profiles measured on $Al_xFe_yNi_{1-x-y}$ CSAFs for $t_{ox} = 0$ h (before oxidation at elevated temperature) have shown that the initial distribution of elemental components is homogeneous across the film cross section. The profiles in Figure 7(a-i) show that the distribution has become very *in*homogeneous by $t_{ox} = 4$ h.

Important phenomenological distinctions can be made between the XPS depth profiles obtained in each of the regions 1-4. The profiles obtained in region 1, Figure 7(a, b, c), show a thin, continuous layer of oxidized Al at the CSAF surface, but no detectable oxidized Fe or Ni at any depth. The profiles from region 2, Figure 7(d, e, f),

appear to show a very thin or partial layer of oxidized Fe and/or Ni below which there is a significant subsurface enrichment of oxidized Al. Below the point of greatest oxidized-Al enrichment, oxidized Fe and Ni are no longer present and the ratio of oxidized-to-metallic Al drops rapidly. The region 3 profiles, Figure 7(g, h), suggest a continuous layer of Fe oxide at the CSAF surface with subsurface enrichment of oxidized Al that is slightly less pronounced than in region 2. A small concentration of oxidized Fe was also detected in both region 3 profiles beyond the point of greatest oxidized Al enrichment. Finally, the region 4 profile, Figure 7(i), (although not indicative of the entire CSAF cross section, since Mo was not detected by the end of the profile) shows a significantly higher amount of total oxide formation than at any of the other locations.

4. DISCUSSION

4.1. Challenges related to the interpretation of this work

It is important to emphasize that that primary intent of this study is to demonstrate our high-throughput methodology as a tool for screening environmental effects on alloy oxidation, for which we have used $Al_xFe_yNi_{1-x-y}$ at 427 °C as a model system. Experimental constraints associated with the RSM-CSAF deposition tool limit the thickness of $Al_xFe_yNi_{1-x-y}$ CSAFs that we can create, which consequently limits the oxidation temperature/time that can be reasonably studied. As a result, it is important to recognize that the direct subject of this study is the oxidation of a very unique system, namely, ~100 nm-thick $Al_xFe_yNi_{1-x-y}$ films that were UHV annealed at 427 °C, exposed briefly to ambient air at room temperature during transfer, and then exposed to humid air at 427 °C for up to 4 h. Thus, interpreting the work as it might relate to other systems poses a number of challenges.

First, with regards to practical applications, oxidation at 427 °C is very early/transient behaviour compared to that typically considered for alumina formers, where bulk alloys may be oxidized in environments at 600 to 1200 °C for hundreds or thousands of hours, sometimes resulting in passivation mechanisms with total oxide layer thicknesses >10 μm [4,12,15,18]. Practical alumina-forming alloys also contain additional components besides Al, Fe, and Ni, generally having a significant Cr content,

and incorporating one or more of a number possible minor components, including Nb, Mo, Mn, W, Y, Hf, Ti, Si, and C, among others [5,15–17]. In principle, developing the ability to prepare much thicker CSAFs with more components could allow high-throughput methods similar to ours to be applied to oxidation studies of alloy composition ranges and oxidizing environments of direct industrial relevance, but this is beyond our current capabilities.

Even when limiting our study to early oxidation, it is unclear how closely the behaviour of various locations on $Al_xFe_yNi_{1-x-y}$ CSAFs might mirror that of bulk alloys with equivalent compositions when exposed to identical conditions. One major reason for this is that there are likely to be significant differences in the grain structure of ~100 nm-thick alloy films compared to bulk alloys, and these differences might affect the oxidation process. Additional work is currently underway to compare the grain structure of $Al_xFe_yNi_{1-x-y}$ CSAFs with that of cast bulk alloys, and to determine how this might influence oxidation at 427 °C. Preliminary results from studies using focused ion beam (FIB) cross-sectioning followed by transmission electron microscopy (TEM) indicate that, after UHV annealing at 427 °C, ~100-150 nm-thick $Al_xFe_yNi_{1-x-y}$ CSAFs are comprised of densely packed, columnar grains with lengths (normal to substrate) of ~80 (±30) nm and widths of ~20 (±5) nm. However, the cast bulk alloys exhibit grains with characteristic dimensions on the order of tens of μm. Such structural differences may be important, particularly if grain boundaries play a significant role in the oxidation process. A related concern is the potential for interactions of the $Al_xFe_yNi_{1-x-y}$ CSAFs with their Mo substrates; however, the preliminary FIB-TEM results have revealed the CSAF to be flat and well-adhered to the substrate at the analysed regions, with interdiffusion limited to an interface region ~2-4 nm in thickness.

A second reason that $Al_xFe_yNi_{1-x-y}$ CSAFs might oxidize differently from bulk alloys is if sufficient oxide formation occurs such that one or more metallic species are significantly depleted from the film, causing a change in its effective composition which affects the subsequent oxidation. Additional work is also underway to investigate the possibility of such depletion effects. Preliminary comparisons made using XPS depth profiling of $Al_xFe_yNi_{1-x-y}$ CSAFs and bulk alloys oxidized under identical conditions at 427 °C have shown very good agreement in the oxide/metal cross sections of Al_xFe_{1-x}

compositions which become passivated by a thin Al_2O_3 scale when oxidized. This suggests that CSAF depletion effects are not significant if passivation occurs during early oxidation. Conversely, depletion effects are likely to factor significantly in the oxidation behaviour of $Al_xFe_yNi_{1-x-y}$ CSAFs in those composition regions which are not passivated and, therefore, are more extensively oxidized.

In light of the considerations above, we did not attempt to characterize in complete detail all of the oxidation mechanisms which occurred across the $Al_xFe_yNi_{1-x-y}$ CSAFs at 427 °C, as it is unlikely that such details are directly relevant to practical applications of alumina-forming alloys. Rather, our interest was in demonstrating the ability of our high-throughput methodology to reveal phenomenological differences in the oxidation occurring across the ternary $Al_xFe_yNi_{1-x-y}$ composition space in different environments. Particularly, we sought to determine whether a $N_{Al}^*(x, y)$ boundary between Al_2O_3-scale passivated and non-passivated compositions could be identified and, if so, whether this boundary was different for oxidation in humid air at 427 °C than that determined in our previous study of oxidation in dry air at 427 °C [23]. The remaining discussion sections proceed as follows. Section 4.2 outlines our phenomenological characterization of the oxidation behaviour of $Al_xFe_yNi_{1-x-y}$ CSAFs in humid air based on the preceding EDX, Raman, and XPS results. In section 4.3, we compare these results to those from our previous study of oxidation in dry air. Finally, in sections 4.4-4.8, we introduce and use a modified version of an established kinetic model to consider whether our studies of early oxidation of $Al_xFe_yNi_{1-x-y}$ CSAFs at 427 °C can offer insights into the physical factors influencing N_{Al}^* in humid vs. dry environments that might also relate to the oxidation of bulk alumina formers at higher temperatures.

4.2. Oxidation behaviour across $Al_xFe_yNi_{1-x-y}$ composition space in humid air at 427 °C

The primary goal of this study was to identify phenomenological differences in early oxidation behaviour across $Al_xFe_yNi_{1-x-y}$ composition space in humid air at 427 °C and to compare this behaviour to that for oxidation in dry air at 427 °C, which we investigated previously while developing the high-throughput methodology [23]. In both

cases, we are ultimately able to directly measure a $N_{\text{Al}}^*(x, y)$, which appears to be the minimum N_{Al} required for the initial establishment of a passivating Al_2O_3 scale during early oxidation at 427 °C. As in our dry-air study, we observed correlations between visually identifiable boundaries on $Al_xFe_yNi_{1-x-y}$ CSAFs oxidized in humid air and transitions between phenomenologically distinct types of oxidation behaviour. The types of behaviour that we propose for the visually distinct regions 1-4 is shown schematically in Figure 8. The schematics in Figure 8 are not presented as rigorously detailed mechanisms for the regions, but are simply meant to emphasize qualitative differences we are able to detect with our characterization methods.

Region 1 contains compositions which were passivated by an exclusive, surface Al_2O_3 scale (Figure 8). The XPS depth profiles from this region (Figure 7(a, b, c)) show that a thin layer (perhaps ~2-4 nm) of continuous oxidized Al is present at the surface of the CSAF, but the majority of the film's cross section remains metallic and uniform in composition. Given the oxidation conditions used in this study, the oxidized Al is likely amorphous Al_2O_3 and/or γ-Al_2O_3, as described in the discussion of region 1 on the CSAFs oxidized in dry air [23]. The EDX measurements of oxygen uptake (Figure 4) revealed that $\Delta C_O \cong 0$ across region 1 for all $t_{ox} > 0$ h, indicating that the compositions in region 1 were passivated against oxidation for the entire 4 h exposure to humid air at 427 °C, and suggesting that the Al_2O_3 was primarily formed during the brief exposure to ambient air at room temperature upon removal from the UHV deposition chamber. The $C_O(t_{ox} = 4\ \text{h})$ in region 1 is the lowest of the four regions because oxygen is only present in the relatively small amount of Al_2O_3 that was formed at the CSAF surface. As mentioned earlier, any Al_2O_3 formed in the CSAFs at 427 °C would not be expected to be Raman-active, which is consistent with the lack of peaks in the Raman spectra measured in region 1 (Figure 6).

The spectroscopic data from region 2 of the CSAFs are consistent with trace Fe and/or Ni oxides on top of a continuous, subsurface Al_2O_3 scale (Figure 8). The depth profiles (Figure 7(d, e, f)) show an initially high concentration of oxidized Fe and/or Ni that rapidly diminishes over the first few etch cycles, revealing a high degree of oxidized Al enrichment in the subsurface. The oxidized Al signal at and below the depth of greatest enrichment must originate primarily from Al_2O_3, as opposed to mixed Al oxides,

since Al is the only oxidized species present in a significant concentration. If the enrichment of oxidized Al is assumed to indicate a thin, continuous layer of subsurface Al_2O_3, then the fact that the depth profiles do not directly reveal a point of 100% oxidized Al in the subsurface suggests that there are lateral variations in the thickness of the Fe/Ni oxides at the surface (potentially to the extent that the Fe/Ni oxides are present as isolated clusters on the Al_2O_3). This type of morphology would prevent the continuous Al_2O_3 scale from being simultaneously exposed to XPS during uniform Ar^+ etching. Given this interpretation of the oxidation behaviour of region 2, the reason for the persistence of a small fraction of oxidized Al at greater depths where the majority of the film cross section is metallic is uncertain; it may arise due to complexities of the CSAF grain structure (see section 4.1), e.g. perhaps as the result of Al_2O_3 formation along columnar grain boundaries. The oxygen uptake measurements (Figure 4), which show $\Delta C_O \cong 0$ from $t_{ox} = 1$ to 4 h, indicate that region 2 became passivated against further oxidation and, therefore, suggest that a continuous Al_2O_3 layer was indeed formed. The $C_O(t_{ox} = 4$ h$)$ is slightly higher in region 2 than in region 1 because of the additional oxygen contained in the trace Fe/Ni oxides. The small, measurable values of ΔC_O from $t_{ox} = 0$ to 1 h shows that some of the oxide formation occurred in the humid air at 427 °C before region 2 was passivated. The $NiFe_2O_4$ phase was detected with Raman spectroscopy (Figure 6) at two of the sampled locations in region 2, but the majority of spectra did not show any peaks, likely because the amount of Fe and/or Ni oxide that was formed was too small to be detected.

Region 3 exhibits oxygen uptake trends (Figure 4) that are nearly identical to region 2: ΔC_O is small, but measurable from $t_{ox} = 0$ to 1 h and $\Delta C_O \cong 0$ from $t_{ox} = 1$ to 4 h. The total $C_O(t_{ox} = 4$ h$)$ is also very similar in both regions. These results suggest that region 3 compositions are also passivated; however, the depth profiles (Figure 7(g, h)) show a slightly lower extent of oxidized-Al enrichment in the subsurface than in region 2, with a continuous layer of oxidized Fe on the CSAF surface. The α-Fe_2O_3 phase was identified with Raman spectroscopy (Figure 6) across all of region 3. Qualitatively equivalent spectroscopic data were obtained across a much larger composition region during our study of $Al_xFe_yNi_{1-x-y}$ CSAF oxidation in dry air at 427 °C [23]. The most likely interpretation is that the compositions in region 3, like region 2, formed a continuous,

passivating Al_2O_3 scale in the subsurface (Figure 8). However, based on the Raman results, the competitive oxide in region 3 appears specifically to be α-Fe_2O_3. Furthermore, the seemingly lower subsurface enrichment of oxidized Al in the XPS depth profiles suggests that there is more variability in the thickness of this competitive oxide in region 3 than in region 2.

Region 4 compositions appear to have experienced internal oxidation in the humid air at 427 °C (Figure 8). The oxygen uptake data (Figure 4) show that $C_O(t_{ox} = 4$ h) is significantly higher across the majority of region 4 than in any of the other regions. The amplified plot of ΔC_O from $t_{ox} = 1$ to 4 h demonstrates clearly that continuing oxygen uptake during this time is exclusively measurable throughout region 4, indicating that passivation did not occur. The depth profile in Figure 7(i) shows that Fe was oxidized extensively, and is very similar in appearance to the depth profile (not included) from the analysis location in the AlFe binary area of region 4 in Figure 7. The two depth profiles (also not included) from near the pure-Ni corner in region 4 revealed significantly less oxidation overall, but did not show any degree of oxidized-Al enrichment in the CSAF cross section that could be indicative of Al_2O_3 scale formation. The Raman analysis (Figure 6) reveals α-Fe_2O_3 transitioning to $NiFe_2O_4$ as the Fe-to-Ni ratio decreases across composition region 4. The appearance of the $NiFe_2O_4$ phase appears to correlate roughly with a rapid decrease in $C_O(t_{ox} = 4$ h) across region 4. Based on the spectroscopic results, we believe that the decrease in $C_O(t_{ox} = 4$ h) as the Fe-to-Ni ratio decreases across region 4 is the result of "pseudo-passivation" (i.e. a very slow growth rate at 427 °C) by $NiFe_2O_4$ and/or NiO, but is not attributable to any type of Al_2O_3 scale formation.

The regions described above subdivide the entire $Al_xFe_yNi_{1-x-y}$ composition space into four phenomenologically distinguishable types of oxidation behaviour that were observed to occur on CSAFs as a result of oxidation in humid air at 427 °C (Figure 8). Composition regions 1, 2, and 3 all become rapidly passivated against oxidation under these conditions due to the formation of an Al_2O_3 scale, but the oxide morphology in each case is unique. In region 1, the Al_2O_3 is exclusive and continuous at the surface of the CSAF. In region 2, the Al_2O_3 forms a continuous layer beneath trace Fe and/or Ni oxides. In region 3, there appears to be a continuous Al_2O_3 layer in the subsurface

beneath variable-thickness α-Fe_2O_3. The compositions in region 4 were not able to establish an Al_2O_3 scale and underwent internal oxidation at a wide range of rates depending on the type of Fe/Ni oxide(s) that were formed. Thus, the boundary of region 4 defines the trajectory of $N_{Al}^*(x, y)$ across $Al_xFe_yNi_{1-x-y}$ composition space for oxidation in the humid air at 427 °C. The $N_{Al}^*(x, y)$ boundary was found to follow a complex path from $Al_{0.35}Fe_{0.65}$ to $Al_{0.22}Ni_{0.78}$, with the minimum being $Al_{0.22}Ni_{0.78}$ and reaching a maximum at $Al_{0.38}Fe_{0.56}Ni_{0.06}$.

4.3. Comparison of $Al_xFe_yNi_{1-x-y}$ oxidation behaviour in dry and humid air at 427 °C

The types of oxidation behaviour identified for composition regions 1-4 of the $Al_xFe_yNi_{1-x-y}$ CSAFs exposed to humid air at 427 °C, as shown in Figure 8, are qualitatively identical to those that we previously identified for the correspondingly numbered regions 1-4 of $Al_xFe_yNi_{1-x-y}$ CSAFs exposed to dry air at the same temperature [23]. Before further comparing the results of the two studies, we amend the composition-space trajectory reported for the transition from region 1 to region 2 in our initial study of dry-air oxidation [23]. As noted earlier and demonstrated by Figure 3(c), the transition from region 1 to region 2 becomes increasingly difficult to identify by visual inspection near the AlNi binary region of the CSAF. This was also observed during our previous visual analyses of the CSAFs oxidized in dry air. Practically speaking, the morphology difference between regions 1 and 2 is minor; both are passivated by an Al_2O_3 scale, but region 2 compositions also have a very small amount of Fe and/or Ni oxide at their surfaces. In fact, of the spectroscopic techniques we have used to study the oxidized CSAFs, only XPS depth profiling is sufficiently surface sensitive to definitively differentiate region 1 from region 2. The use of a relatively smaller number of XPS depth profile locations on the dry-air-oxidized CSAFs meant that the visually determined placement of the boundary between regions 1 and 2 could not be confirmed as precisely as the other boundaries, which were verified by the higher-density EDX or Raman measurements. However, we discovered during the study of CSAF oxidation in humid air that the transition from region 1 to region 2 can be easily discerned across the entire $Al_xFe_yNi_{1-x-y}$ composition space using SEM contrast, as shown in Figure 3(d). Thus, formerly acquired SEM images of the dry-air-oxidized CSAFs described in our

previous study were used to reassess the trajectory of the boundary between regions 1 and 2 near the AlNi binary region of composition space. Figure 9 shows the resulting adjustment for one of the CSAFs and the updated behaviour map of composition regions 1-4 for dry-air oxidation at 427 °C. The dotted line shows our originally proposed boundary between regions 1 and 2 determined by visual analysis of the photograph [23]. The solid line shows the newly determined path of this boundary based on the readily observable contrast difference in the SEM image. The new trajectory only begins to diverge from the initially determined trajectory near the AlNi binary. Consequently, we believe that region 2 extends to higher Al concentrations along the AlNi binary than we previously reported for oxidation in dry air at 427 °C, but it should again be emphasized that the distinction between regions 1 and 2 is quite subtle.

In view of the amended boundary shown in Figure 9, the results of our studies on $Al_xFe_yNi_{1-x-y}$ CSAF oxidation in dry air and humid air at 427 °C can be directly compared. Figure 10 shows a photograph, the C_O measured by EDX, and the Raman phase map for one CSAF exposed to dry air and one exposed to humid air, each for $t_{ox} = 4$ h. While many aspects of the visual appearance (Figure 10(a)) are similar in the two cases, there are significant differences in the surface colouration patterns in regions 3 and 4. By comparing $C_O(t_{ox} = 4$ h) in the ternary composition diagrams (Figure 10(b)), it is immediately apparent that the rapid increase in C_O upon crossing into region 4 (correlating to the transition from internal to external oxidation) is shifted to significantly higher Al contents at high Fe-to-Ni ratios for the CSAF exposed to humid air. While the C_O plots suggest that certain compositions are oxidized to a markedly different extent in the two different environments, the Raman phase maps (Figure 10(c)) show that the oxide phases that are formed in the different regions of composition space in either case are quite similar. The overall strength of the Raman signal measured at the various surface locations was observed to be substantially higher for the CSAF oxidized in dry air than for the CSAF oxidized in humid air, despite identical acquisition conditions. The reason for this difference is not known, but the much lower signal-to-noise ratio in the data collected on the CSAF oxidized in humid air may have prevented identification of spectra that were definitively characteristic of NiO along the AlNi binary

of region 4, as the single peak assigned to NiO in the dry-air study was very low and broad compared to those observed for the other oxide phases [23].

The depth resolution of the XPS depth profiles presented in this study (Figure 7) is higher by a factor of ~3× than that of those obtained in our previous study of CSAF oxidation in dry air [23]. Depth profiles are not directly compared in Figure 10 for the sake of space, but the key qualitative features (as described earlier in section 4.2) were the same within each corresponding region, 1-4, of the CSAFs oxidized in the two different environments. While the procedure for peak fitting the XPS data obtained in this study (Appendix A) was slightly more sophisticated than that used in our previous study [23], the effect of reprocessing the previously obtained XPS depth-profile data using the new peak-fitting method was found to be minimal. The calculated ratio of oxidized-to-metallic species in regions where both are present was marginally reduced as a result of fitting the metallic peaks with a slight tail at higher binding energies. However, the qualitative aspects of the profiles used to infer oxidation phenomenology remained unchanged.

The results of our spectroscopic analyses of $Al_xFe_yNi_{1-x-y}$ CSAFs suggest that the four types of phenomenologically distinguishable oxidation behaviour shown in Figure 8 occur in both dry air and humid air at 427 °C. Figure 11 shows a comparison of the composition-space trajectories determined for the boundaries demarcating the transitions between the regions 1-4 in each case. The boundaries are plotted in a rectangular representation of $Al_xFe_yNi_{1-x-y}$ composition space with N_{Al} plotted as a function of $N_{Fe} / (N_{Fe} + N_{Ni})$. The vertical and horizontal error bars show uncertainty in position based on the calculated precision of the visual analysis technique used to translate the boundaries from real space into composition space. From this comparison, it can be seen that the only measurably significant difference between the two oxidizing environments is a shift in the boundary between regions 3 and 4. Region 3 is significantly narrower for oxidation in humid air than in dry air, being largely supplanted by an expansion of region 4. Thus, the only relevant difference between the two environments is in the subset of $N_{Al}^*(x, y)$ which separates regions 3 and 4. Figure 12 shows a comparison of the $N_{Al}^*(x, y)$ boundaries determined for exposure at 427 °C to dry air and humid air. The boundaries are plotted in both the rectangular representation

of Al$_x$Fe$_y$Ni$_{1-x-y}$ composition space with error bars, and in a typical ternary composition diagram without error bars. At low Fe-to-Ni ratios, $N_{\text{Al}}^*(x, y)$ is approximately constant at ~0.23 in both environments. The values of $N_{\text{Al}}^*(x, y)$ in dry and in humid air begin to measurably diverge at $N_{\text{Fe}} / (N_{\text{Fe}} + N_{\text{Ni}}) \cong 0.35$. The magnitude of this divergence increases rapidly beginning at ~0.55, and appears to reach a maximum at ~0.85, where $N_{\text{Al}}^* \cong 0.15$ in dry air and $N_{\text{Al}}^* \cong 0.37$ in humid air. As demonstrated in Figure 11, the increase of N_{Al}^* in humid air compared to dry air appears to manifest itself as a collapsing of region 3 in favour of region 4, i.e. many Al$_x$Fe$_y$Ni$_{1-x-y}$ compositions on a CSAF that are passivated by a subsurface Al$_2$O$_3$ scale beneath a continuous surface layer of α-Fe$_2$O$_3$ as a result of oxidation in dry air at 427 °C instead experience extensive internal oxidation when exposed to humid air at 427 °C.

4.4. Wagner-Maak kinetic model of oxidation and N_{Al}^* in Al alloys

As mentioned earlier, our measured $N_{\text{Al}}^*(x, y)$ trajectories (shown in Figure 12) appear to be the minimum Al content required for initial establishment of a continuous, protective Al$_2$O$_3$ scale in Al$_x$Fe$_y$Ni$_{1-x-y}$ alloys at 427 °C. We now attempt to analyse our results in terms of a kinetic model for alloy oxidation to consider whether they can offer insights into the physical origins of the composition- and humidity-dependent variations in the value of N_{Al}^* observed for early oxidation of our Al$_x$Fe$_y$Ni$_{1-x-y}$ CSAFs at 427 °C, which may also relate to the oxidation of bulk alloys at higher temperature. To the best of our knowledge, the only theoretical treatment commonly applied to predict the critical component concentration required for passivating scale establishment is based on a quantitative criterion that was developed for binary alloy systems by Wagner [27]. Wagner's model describes the system in terms of one-dimensional counter-diffusion of oxygen against the alloy component that is oxidized to form the passivating scale. Therefore, applicability of the model requires that the oxidation process be controlled by diffusion. Whether or not this is the case for our studies of Al$_x$Fe$_y$Ni$_{1-x-y}$ CSAF oxidation at 427 °C will be discussed in more detail later. Acknowledging this possible limitation, we move forward in considering how the model might be applied to interpreting our results.

A significant practical drawback to Wagner's model is that it assumes that the only metal that is oxidized in the process is the one which forms the passivating scale, i.e. the oxide of the other alloy component is not stable under the oxidizing conditions. An extension was later applied to the model by Maak in an attempt to account for more practically relevant situations where there is competitive formation of a non-protective oxide of the other metal component [28]. The assumptions and derivation of the Wagner and Wagner-Maak models have been adeptly summarized by other authors [8,29]. In the remainder of this report, we review the derivation of the Wagner-Maak model, suggest two minor modifications, consider its applicability to our $Al_xFe_yNi_{1-x-y}$ CSAF oxidation data, and analyse which kinetic parameters could explain the composition- and humidity-dependent variations we have observed in the value of N_{Al}^* assuming that the model can be applied to our system.

We review the derivation of the Wagner-Maak model here, but specifically consider a case involving oxidation of an AlM alloy, where M is a generic metal component which forms a competitive oxide MO_β. A schematic showing the cross section of an oxidized AlM alloy as described by the Wagner-Maak model is shown in Figure 13. The model predicts time-dependent advancement in depth into the alloy, z, of two distinct oxidation fronts, where $z = 0$ represents the position of the alloy/gas interface prior to any oxidation. The front at $z = \xi$ is the leading edge of the internal oxidation zone (IOZ) in which all metallic Al is assumed to have been converted to Al_2O_3 precipitates. The front at $z = X$ is the depth of inward advancement of competitive MO_β formation. For scale passivation to be possible, Al_2O_3 must be more thermodynamically stable than MO_β, i.e. Al_2O_3 must be the only oxide that can form once the local oxygen chemical potential decreases below some threshold with increasing depth into the alloy. Thus, the model is only physically meaningful if $\xi > X$. The two oxidation fronts are assumed to advance according to parabolic rate laws of the form

$$X^2 = 2k_c t \qquad (1)$$

$$\xi^2 = 4\gamma^2 D_O t \qquad (2)$$

where t is time, k_c is a rate constant for the inward part of the competitive MO_β scale growth from $z = 0$, D_O is the diffusion coefficient of oxygen in metallic M, and γ is a dimensionless parameter related to a rate constant for advancement of the IOZ. The metallic M matrix is assumed to be immobile. Concentration profiles for Al and oxygen are determined by applying the one-dimensional diffusion equations

$$\frac{\partial N_O}{\partial t} = D_O \frac{\partial^2 N_O}{\partial z^2} \tag{3}$$

$$\frac{\partial N_{Al}}{\partial t} = D_{Al} \frac{\partial^2 N_{Al}}{\partial z^2} \tag{4}$$

where N_O and N_{Al} are the mole fractions of oxygen and Al, respectively, and D_{Al} is the diffusion coefficient of Al in metallic M. Based on the assumptions of the model, the boundary conditions are

$$N_{Al} = N_{Al}^{(0)} \quad \text{for} \quad z \geq 0, \ t = 0 \tag{5}$$

$$N_O = 0 \quad \text{for} \quad z \geq \xi, \ t > 0 \tag{6}$$

$$N_{Al} = 0 \quad \text{for} \quad z \leq \xi, \ t > 0 \tag{7}$$

$$N_O = N_O^{(s)} \quad \text{for} \quad z = X, \ t > 0 \tag{8}$$

where $N_O^{(s)}$ is the initial ($t = 0$) equilibrium oxygen solubility (in mole fraction) in metallic M at the alloy/gas interface ($z = 0$) and $N_{Al}^{(0)}$ is the Al concentration (mole fraction) in the bulk alloy. The boundary condition in Equation 5 stipulates that, prior to oxidation, the alloy is uniform in composition at all depths. The remaining boundary conditions are defined based on the positions of the oxidation fronts, X and ξ, which are time dependent. The boundary conditions in Equations 6 and 7 establish the assumptions that no oxygen is present in the alloy at $z \geq \xi$, and that all metallic Al has been depleted

at $z \leq \xi$ (by conversion to Al_2O_3). Finally, the boundary condition in Equation 8 states that the initial mole fraction of oxygen in M at the alloy surface is maintained at the advancing front of the MO_β scale, i.e. that the competitive oxide acts as an infinitely fast "short-circuit" route for oxygen diffusion to the MO_β /IOZ interface, allowing equilibrium with the oxygen partial pressure in the gas phase to be maintained at $z = X$ for all t. The solutions for the oxygen and Al mole fraction profiles based on Equations 1-8 are given by

$$N_O = N_O^{(s)} \frac{\mathrm{erf}(\gamma) - \mathrm{erf}\left(\frac{z}{2\sqrt{D_O t}}\right)}{\mathrm{erf}(\gamma) - \mathrm{erf}(u)} \quad \text{for} \quad X \leq z \leq \xi \tag{9}$$

$$N_{Al} = N_{Al}^{(0)} \left[1 - \frac{\mathrm{erfc}\left(\frac{z}{2\sqrt{D_{Al} t}}\right)}{\mathrm{erfc}(\gamma\sqrt{\varphi})}\right] \quad \text{for} \quad z \geq \xi \tag{10}$$

where u and φ are defined as

$$u = \sqrt{\frac{k_c}{2D_O}}$$

$$\varphi = \frac{D_O}{D_{Al}}$$

The Wagner-Maak model assumes that all precipitation of Al_2O_3 occurs at ξ and, thus, that the molar fluxes of oxygen and Al arriving at ξ as a result of diffusion must satisfy this stoichiometry. This is expressed mathematically as

$$\lim_{\varepsilon \to 0} \left(-D_O \left(\frac{\partial N_O}{\partial z}\right)_{z=\xi-\varepsilon}\right) = \lim_{\varepsilon \to 0} \left(\nu D_{Al} \left(\frac{\partial N_{Al}}{\partial z}\right)_{z=\xi+\varepsilon}\right) \tag{11}$$

where v is the stoichiometric constant describing the oxygen-to-Al ratio in the Al oxide that is being formed (in an ideal case where Al is oxidized only to Al_2O_3, $v = 1.5$). Equation 11 can be solved by substituting Equations 9 and 10 to obtain

$$\frac{N_O^{(s)}}{vN_{Al}^{(0)}} = \frac{erf(\gamma)-erf(u)}{erf(\gamma)}\frac{G(\gamma)}{F(\gamma\varphi^{1/2})} \tag{12}$$

where $G(\gamma)$ and $F(\gamma\varphi^{1/2})$ are defined as

$$G(\gamma) = \pi^{1/2}\gamma\exp(\gamma^2)\,erf(\gamma)$$

$$F(\gamma\varphi^{1/2}) = \pi^{1/2}\gamma\varphi^{1/2}\exp(\gamma^2\varphi)\,erfc(\gamma\varphi^{1/2})$$

Equation 12 describes only an ongoing internal oxidation process as shown in Figure 13. The Wagner-Maak model is used to predict N_{Al}^* by first writing a mass balance on the Al contained in the Al_2O_3 (i.e. AlO_v) that is precipitated at ξ of the form

$$N_{AlO_v}\left(\frac{d\xi}{dt}\right) = \lim_{\varepsilon\to 0}\left(D_{Al}\frac{\partial N_{Al}}{\partial z}\right)_{z=\xi+\varepsilon} \tag{13}$$

where N_{AlO_v} is a constant mole fraction of AlO_v precipitated in the IOZ. Equation 13 can be solved by substituting Equations 2 and 10 to obtain

$$N_{AlO_v} = \frac{N_{Al}^{(0)}}{F(\gamma\varphi^{1/2})} \tag{14}$$

An "enrichment factor" of Al is defined as

$$\alpha = \frac{N_{AlO_v}}{N_{Al}^{(0)}} = \frac{1}{F(\gamma\varphi^{1/2})} \tag{15}$$

The crucial assumption made by Wagner is that one can define a quantity, g^*, describing a critical volume fraction of AlO_v forming in the IOZ, above which inward oxygen diffusion will be "sufficiently reduced" (due to blocking by the Al_2O_3 precipitates) such that lateral growth begins to dominate and a continuous, passivating Al_2O_3 layer is established. Wagner related g^* to N_{AlO_v} by the expression

$$N_{AlO_v} = g^* \left(\frac{V_M}{V_{ox}} \right) \tag{16}$$

where V_M and V_{ox} are the molar volumes of M and AlO_v, respectively. Thus, N_{Al}^* is given by the value of $N_{Al}^{(0)}$ which yields a value of N_{AlO_v} (Equation 14) that satisfies Equation 16. Equations 15 and 16 are combined to obtain

$$N_{Al}^* = g^* \left(\frac{V_M}{V_{ox}} \right) F(\gamma \varphi^{1/2}) \tag{17}$$

which is posed simultaneously with Equation 12 (with N_{Al}^* substituted for $N_{Al}^{(0)}$)

$$\frac{N_O^{(s)}}{\nu N_{Al}^*} = \frac{\mathrm{erf}(\gamma) - \mathrm{erf}(u)}{\mathrm{erf}(\gamma)} \frac{G(\gamma)}{F(\gamma \varphi^{1/2})} \tag{18}$$

to yield the final mathematical form of the Wagner-Maak model. Equations 17 and 18 can be solved simultaneously for any two of the variables N_{Al}^*, $N_O^{(s)}$, D_O, D_{Al}, g^*, k_c, V_M, V_{ox}, ν, and γ, given appropriate values of the others. Ideally, given values for the physically defined quantities $N_O^{(s)}$, D_O, D_{Al}, g^*, k_c, V_M, V_{ox}, and ν, one could solve for γ (which is defined only by the model) and then predict the value of N_{Al}^*.

4.5. Modified Wagner-Maak model for limiting cases where $g^* \to 1$

Accepting the simplifying assumptions described above, the Wagner-Maak model produces a physically intuitive description of the internal oxidation mechanism shown in Figure 13, provided that the values of N_{Al}^* and g^* are small. However, clearly

unphysical situations are predicted when considering limiting values of N_{Al}^* and g^*, which lead us to make two minor modifications to the definitions of these parameters used in the Wagner-Maak model.

The first modification is to the relationship established in Equation 16 between the critical AlO_v volume fraction, g^*, and the AlO_v mole fraction, N_{AlO_v}. For a fixed number of moles in a system containing only immiscible AlO_v and M, the precise relationship between the defined value of g^* and N_{AlO_v} is

$$N_{AlO_v} = \left(\frac{g^* V_M}{V_{ox} + g^* V_M - g^* V_{ox}} \right) \tag{19}$$

If V_M and V_{ox} differ significantly, Equation 16 is approximately equivalent to Equation 19 only when the value of g^* is small. Figure 14 shows a comparison of the relationship between N_{AlO_v} and g^* according to Equations 16 and 19 when $V_{ox} = 1.9 V_M$ (representative of the approximate molar volume ratio for an $AlO_{1.5}$ and Ni binary system). The values of N_{AlO_v} predicted by the two equations diverge as the value of g^* increases. As a consequence of using Equation 16, the actual value of N_{AlO_v} that corresponds to a specific value of g^* is increasingly underestimated as g^* increases. The Wagner-Maak model assumes that N_{AlO_v} is equal to the effective Al mole fraction obtained due to diffusive Al enrichment at $z = \xi$ immediately before the Al_2O_3 is formed (i.e. $N_{AlO_v} = \alpha N_{Al}^{(0)}$). Under this assumption, N_{Al}^* will also be increasingly underestimated as g^* increases as a result of using Equation 16. From a practical standpoint, it has been shown by Yi et al. [30] that stresses resulting from volume expansion during Al_2O_3 formation in AlNi alloys cause preferential displacement of Ni to the alloy surface, which would offset this error since the resulting N_{AlO_v} in the subsurface would actually be greater than $\alpha N_{Al}^{(0)}$. However, the extent to which preferential displacement of M might factor into other AIM systems is not clear. Furthermore, Equation 19 sets a physically intuitive limiting bound as $g^* \rightarrow 1$, requiring that an Al_2O_3 volume fraction of 1 correspond to an Al_2O_3 mole fraction of 1.

Our second modification to the Wagner-Maak model relates to how the diffusive enrichment of Al is defined. Writing Equation 4 in terms of Al mole fraction is appropriate when the value of $N_{Al}^{(0)}$ is small. However, given the model's assumption that the M matrix is immobile, this treatment becomes increasingly erroneous as the value of either $N_{Al}^{(0)}$ or α increases. For example, even if Equation 19 is used in place of Equation 16, the limiting case where $g^* = N_{AlO_v} = 1$ can still result in counterintuitive solutions where $\alpha > 1$, and $N_{Al}^* < 1$ as a result. This concern can be addressed by writing Equations 3-8, 11, and 13 in terms of concentrations rather than mole fractions, i.e. by replacing all instances of N with c, where c_i is the concentration of species i in units of moles per volume. Equation 12 then becomes

$$\frac{c_O^{(s)}}{v c_{Al}^{(0)}} = \frac{erf(\gamma) - erf(u)}{erf(\gamma)} \frac{G(\gamma)}{F(\gamma \varphi^{1/2})} \tag{20}$$

where $G(\gamma)$ and $F(\gamma \varphi^{1/2})$ are defined as before. Likewise, Equation 14 becomes

$$c_{AlO_v} = \frac{c_{Al}^{(0)}}{F(\gamma \varphi^{1/2})} \tag{21}$$

and the Al enrichment factor, formerly expressed by Equation 15, is now defined as

$$\alpha = \frac{c_{AlO_v}}{c_{Al}^{(0)}} = \frac{1}{F(\gamma \varphi^{1/2})} \tag{22}$$

Equations 20-22 can be rewritten in terms of mole fractions by assuming

$$N_{Al} = \frac{c_{Al}}{c_{Al} + c_M} \tag{23}$$

where c_M is the molar concentration of immobile M in the metallic matrix. Neglecting volume expansion due to diffusive Al enrichment, the value of c_M can be assumed to be

constant. It is reasonable to assume that $N_O^{(s)} \ll 1$, so N_O can be accurately approximated as

$$N_O = \frac{c_O}{c_M} \qquad (24)$$

Equations 19-24 can be combined and rearranged to yield a modified Wagner-Maak model of the form

$$\frac{N_{Al}^*}{N_{Al}^* + F(\gamma \varphi^{1/2})(1 - N_{Al}^*)} = \frac{g^* V_M}{V_{ox} + g^* V_M - g^* V_{ox}} \qquad (25)$$

$$\frac{N_O^{(s)}(1 - N_{Al}^*)}{\nu N_{Al}^*} = \frac{\text{erf}(\gamma) - \text{erf}(u)}{\text{erf}(\gamma)} \frac{G(\gamma)}{F(\gamma \varphi^{1/2})} \qquad (26)$$

As with the unmodified Wagner-Maak model (Equations 17 and 18), Equations 25 and 26 can be solved simultaneously for any two of the variables N_{Al}^*, $N_O^{(s)}$, D_O, D_{Al}, g^*, k_c, V_M, V_{ox}, ν, and γ, given appropriate values of the others. Inspection of Equations 25 and 26 reveals that they become equivalent to Equations 17 and 18 in the limit of small values of N_{Al}^* and g^*. In practice, the predictions of the modified and unmodified Wagner-Maak models are fairly similar for small to moderate values of these variables. Neither model incorporates details of volume expansion related to oxide formation or Al diffusion, but the modified form has the advantage of forcing the intuitively correct limiting solution that $N_{Al}^* \rightarrow 1$ as the specified value of $g^* \rightarrow 1$.

4.6. Applying the Wagner-Maak model to the $Al_xFe_yNi_{1-x-y}$ CSAF oxidation results

A number of the details of the Wagner-Maak model must be considered to assess its ability to describe the results of our oxidation studies on $Al_xFe_yNi_{1-x-y}$ CSAFs. Most importantly, as stated earlier, the oxidation process must be diffusion-controlled for the model to apply. Typically, it has been applied to alloy systems at temperatures >800 °C where this is known to be the case. The best indication of whether diffusion is also controlling the oxidation of our $Al_xFe_yNi_{1-x-y}$ CSAFs at 427 °C would be if our

measurements of C_O vs. time exhibited parabolic trends. However, due to practical limitations of these measurements (primarily the reasonably achievable number and spacing of time points), it is not possible for us to definitively determine whether or not this is so. We proceed recognizing the possibility that, if the oxidation process is driven by a mechanism other than diffusion in our $Al_xFe_yNi_{1-x-y}$ CSAFs at 427 °C, the conclusions drawn by analysis using any Wagner-Maak-based model may not be accurate.

Another important point is that for an alloy with a subcritical Al content, the Wagner-Maak model predicts ongoing, time-dependent internal oxidation as depicted in Figure 13 (based on the variables $N_{Al}^{(0)}$, $N_O^{(s)}$, D_O, D_{Al}, k_c, ν, and γ as defined by Equations 1, 2, and 12). Thus, for the oxidation behaviour of the $Al_xFe_yNi_{1-x-y}$ CSAFs to be consistent with the Wagner-Maak model requires that the oxide cross section for $N_{Al}^{(0)} < N_{Al}^*$ resemble that shown in Figure 13. This appears to be generally consistent with the XPS depth profile shown in Figure 7(i) of one such location on a CSAF oxidized in humid air. The profile reveals a continuous layer of competitive Fe oxide at the CSAF surface, transitioning to a combination of oxidized Fe and oxidized Al with increasing depth. It is not necessary that the profile reveal regions corresponding to $X \leq z \leq \xi$ and $z \geq \xi$ in Figure 13 to be consistent with this description of oxidation behaviour, since ξ and X must eventually exceed the limits of the initial CSAF thickness if passivation does not occur. It should be noted that the surface layer of 100% MO_β shown for $z < 0$ in Figure 13 is not directly described in the mathematics of the Wagner-Maak model, although it is a well-known feature of the oxide morphology developed on AIM alloys when M can be oxidized and $N_{Al}^{(0)} < N_{Al}^*$ [8,10,20]. Based on the model's assumption that an oxygen mole fraction $N_O^{(s)}$ is maintained at X for all $t > 0$, the impact of the competitive MO_β formation on the predicted value of N_{Al}^* depends solely on the value of k_c, which describes only the growth of the inner part of the MO_β scale. Practically speaking, the thickness of the outer MO_β scale and the value of k_c will be related.

Given that the Wagner-Maak model is derived based on the assumption of a semi-infinite bulk, it is also prudent to consider whether preferential depletion of one or more metallic components from the non-infinite CSAF during oxide formation might

affect its assumptions or boundary conditions. As discussed earlier (section 4.1), additional work is underway to investigate possible depletion effects by comparing the oxidation of CSAFs with that of bulk alloys, and our preliminary results suggest that CSAF depletion is not significant when Al_2O_3 passivation occurs during early oxidation. Since our CSAF studies reveal a clear shift from passivated to non-passivated compositions, and our goal is simply to use the Wagner-Maak model to gain insights related to the N_{Al}^* where this transition takes place, it appears that concerns related to depletion effects are minimal.

Finally, it is important to recall that the Wagner-Maak model is only related to N_{Al}^* by Wagner's assumption regarding g, the volume fraction of Al_2O_3 being formed in the IOZ. If $g < g^*$, precipitate blocking of oxygen diffusion is assumed to be negligible, but if $g \geq g^*$, it is assumed to be the controlling factor that causes a passivating scale to be established. Thus, the strict physical picture of the model is that an AIM alloy with $N_{Al}^{(0)} < N_{Al}^*$ will experience ongoing internal oxidation with a morphology like that shown in Figure 13, while an alloy with $N_{Al}^{(0)} \geq N_{Al}^*$ will develop a passivating Al_2O_3 scale instead. In this respect, the results of our oxidation studies again seem to be quite consistent with the model, as we have been able to observe sharply defined $N_{Al}^*(x, y)$ boundaries on $Al_xFe_yNi_{1-x-y}$ CSAFs oxidized in either dry or humid air. This is particularly well illustrated by the plot of $C_O(t_{ox} = 4 \text{ h})$ in Figure 4, which shows that the total oxygen uptake into the CSAF was increased by a factor of ~4× over a range of just a few at.% Al upon transitioning from the passivated region 3 to the non-passivated region 4. No distinction is made by the Wagner-Maak model as to whether the passivating Al_2O_3 scale will be established at the surface or in the subsurface if $N_{Al}^{(0)} \geq N_{Al}^*$.

Although the basic physical picture of the Wagner-Maak model appears to be essentially correct for diffusion-controlled oxidation, it has never been demonstrated that it can provide predictions of the value of N_{Al}^* that are sufficiently accurate for alloy design, even in alloy systems where this is definitively known to occur. This is likely due, in part, to difficulties associated with accurately determining the values of the various kinetic parameters contained in the model. The parameters, as described in the derivation of Equations 17 and 18, would be most appropriately applied to modelling the

oxidation of a large AlM single crystal where $N_{\mathrm{Al}}^{(0)}$ is small. However, complications arise when considering less ideal systems. For example, in a polycrystalline alloy, oxygen and Al are likely to diffuse at different rates through the crystalline matrix, at grain boundaries, and/or along Al_2O_3/M interfaces [31,32]. Furthermore, certain AlM alloy compositions form coexisting phases which could have significantly different local compositions and/or kinetic properties. The Wagner-Maak model can only be quantitatively accurate if it is possible to determine an appropriate "effective value" for each kinetic parameter which account for these types of effects. However, for the purposes of analysing our data, this also means that the model can be extended from binary AlM to consider the more complex AlFeNi system if M is assumed to be a variable mixture of Fe and Ni, where the effective parameter values depend on the Fe-to-Ni ratio.

4.7. Sensitivity analysis of N_{Al}^{*} to parameters in modified Wagner-Maak model

Without known values for the parameters $N_{\mathrm{O}}^{(s)}$, D_{O}, D_{Al}, k_c, and g^*, we performed a simple sensitivity analysis to investigate their influence on the value of N_{Al}^{*} predicted by the modified Wagner-Maak model. This sensitivity analysis is not a mathematically rigorous screening of the full parameter space but, rather, is intended to provide physical insights into the effects of each parameter. For the analysis, we chose wide ranges of possible "effective values" of these parameters for AlFeNi oxidation at 427 °C. Equations 25 and 26 were then repeatedly solved to find N_{Al}^{*} and γ across the range of values selected for each parameter while holding all of the other variables constant at a chosen set of base values. The base value and range for each variable are shown in Table 1. The base values of V_{M} and V_{ox} in Table 1 correspond to the approximate molar volumes at 427 °C of metallic Ni and $AlO_{1.5}$, respectively. The value of v was taken as 1.5 (the stoichiometric ratio of oxygen-to-Al in Al_2O_3). The base values of $N_{\mathrm{O}}^{(s)}$, D_{O}, and D_{Al} are intended to be roughly appropriate for a Ni single-crystal matrix in equilibrium with NiO at 427 °C, and were obtained by extrapolating (to the nearest order of magnitude) from temperature dependences of these parameters that have been measured by other authors [33–36]. The base value of k_c was then chosen (to the

nearest order of magnitude) to maximize the sensitivity of the predicted value of N_{Al}^* to small changes in the value of k_c. Finally, the base value of g^* was chosen such that the N_{Al}^* predicted using the complete set of base values in Table 1 was in agreement with that which we experimentally observed at the AlNi binary using the Al$_x$Fe$_y$Ni$_{1-x-y}$ CSAFs (as shown in Figure 12, this N_{Al}^* value was very similar in both the dry-air and humid-air environments).

Plots of the N_{Al}^* predicted by the modified Wagner-Maak model across the ranges of values of $N_0^{(s)}$, D_0, D_{Al}, k_c, and g^* shown in Table 1 are presented in Figure 15. The point shown as an open circle on each plot indicates the N_{Al}^* calculated for the complete set of base values shown in Table 1. The solid points show the N_{Al}^* calculated for different values of the parameter on the horizontal axis while holding all of the other parameters constant at their base values. The modified functional form of the Wagner-Maak model was used because of the extreme limiting values that were considered for g^*. As mentioned earlier, the predictions of the modified and unmodified model are similar unless the values of g^* or N_{Al}^* are large, and thus the plot of N_{Al}^* vs. g^* (Figure 15(e)) is the only one that is significantly affected by the choice of the modified model (the unmodified-model solutions converge to $N_{Al}^* \cong 0.43$ at $g^* = 1$, rather than $N_{Al}^* = 1$). The predicted N_{Al}^* values shown on the other plots (Figure 15(a-d)) are systematically decreased by between 0.03 and 0.05 if the unmodified model is used, but the general trends remain identical. The plots in Figure 15 allow assessment of the manner in which the effective values of the kinetic parameters of the modified Wagner-Maak model affect the predicted value of N_{Al}^*.

The plots showing calculated N_{Al}^* as a function of $N_0^{(s)}$ and D_0 (Figure 15(a, b)) reveal an identical trend if either is increased or decreased by an equivalent factor relative to its base value. The predicted values of N_{Al}^* fall on S-shaped curves, approaching a non-zero, asymptotic limit for both high and low extremes of $N_0^{(s)}$ or D_0. In the limit of low $N_0^{(s)}$ or D_0 values, inward oxygen diffusion becomes negligibly slow relative to outward Al diffusion, maximizing the degree to which Al is enriched at $z = \xi$ before forming Al$_2$O$_3$ (see Figure 13). The solution does not converge to $N_{Al}^* = 0$ in the limit of low $N_0^{(s)}$ or D_0 values because the timescale for Al enrichment is still restricted

by growth of the competitive MO$_\beta$ scale, i.e. the specific solution that $N_{Al}^* \cong 0.19$ results from a balance between the base values of D_{Al} and k_c. Conversely, in the limits of high $N_O^{(s)}$ or D_O values, outward Al diffusion becomes negligibly slow relative to inward oxygen diffusion. In such a situation, Al is essentially immobile and diffuses at a rate which is insufficient to allow for any significant enrichment at $z = \xi$ before the Al$_2$O$_3$ is formed (i.e. $\alpha = 1$). It is, therefore, required that $N_{Al}^* = N_{AlO_\nu}$ to obtain an oxide volume fraction of g^* and satisfy the modified Wagner-Maak criterion. In this case, N_{Al}^* may simply be calculated directly from Equation 19, which depends only on g^*, V_M, and V_{ox}. Inserting the base values for these three parameters into Equation 19, one obtains $N_{AlO_\nu} \cong 0.26$, which is the asymptotic limit of the predicted value of N_{Al}^* at high values of $N_O^{(s)}$ or D_O.

The plot showing calculated N_{Al}^* vs. D_{Al} (Figure 15(c)) also exhibits an S-shaped trend. In the limit of low D_{Al} values, outward Al diffusion is again negligibly slow relative to inward oxygen diffusion. This is another scenario in which there is no significant Al enrichment, and an asymptotic limit is obtained that is identical to that observed for high $N_O^{(s)}$ or D_O values (again, determined by Equation 19 and depending only on the values of g^*, V_M, and V_{ox}). In the limit of high D_{Al} values, the value of N_{Al}^* calculated from the modified Wagner-Maak model asymptotically approaches 0. This is because as D_{Al} increases, Al diffusion becomes fast relative to both oxygen diffusion and the competitive MO$_\beta$ scale growth rate, causing the degree of predicted Al enrichment to continuously increase as D_{Al} is increased.

The plot of calculated N_{Al}^* as a function of k_c (Figure 15(d)) shows another S-shaped trend where both asymptotic limits are non-zero. In the limit of low k_c values, the growth rate of the competitive scale becomes negligibly slow relative to the diffusion rates of Al and oxygen. As a result, $X \ll \xi$ (see Figure 13), i.e. competitive MO$_\beta$ scale growth is negligible. In this case, the timescale for Al enrichment is restricted only by the rate of inward oxygen diffusion, and the specific solution that $N_{Al}^* \cong 0.21$ results from a balance between the base values of $N_O^{(s)}$, D_O, and D_{Al}. In the limit of high k_c values, the diffusion rates of Al and oxygen become negligibly slow relative to the competitive scale growth rate. As in the case of high $N_O^{(s)}$, high D_O, or low D_{Al}, no significant enrichment of

Al is able to occur, and direct conversion of the initial Al content to Al_2O_3 must result in the volume fraction g^* (as defined by Equation 19) for passivation to occur.

The plot in Figure 15(e) shows that the N_{Al}^* predicted by the modified Wagner-Maak model can be made to range anywhere from 0 to 1 for values of the critical Al_2O_3 volume fraction, g^*, lying between 0 to 1. Given the manner in which g^* is physically described by Wagner, we believe that this is a more intuitive result than that suggested by the unmodified model. Due to the limitations of Equation 16, the unmodified Wagner-Maak model will converge to a predicted value of N_{Al}^* which is no greater than V_M/V_{ox} as $g^* \to 1$.

The influence of V_M and v on the values of N_{Al}^* predicted by the modified Wagner-Maak model were also investigated, but are not shown in Figure 15. Because V_M would be expected to vary with $Al_xFe_yNi_{1-x-y}$ composition, it was allowed to increase from the base value of 6.7 cm^3/mol up to 7.2 cm^3/mol (the approximate molar volume of pure Fe at 427 °C), but the predicted value of N_{Al}^* was only found to vary by ~0.01 across this range. The parameter v was investigated because, as discussed in detail by Meijering [37], its effective value can change if the metal component forming the protective oxide also forms a mixed oxide with another alloy component, a condition which might arise in the $Al_xFe_yNi_{1-x-y}$ system. In AlNi alloys, the effective value of v has been found to be ~2 due to $NiAl_2O_4$ formation [20]. However, changing v from the base value of 1.5 to 2.0 was found to change the N_{Al}^* predicted by the modified Wagner-Maak model by <0.005. Thus, if the modified Wagner-Maak model can be applied to our $Al_xFe_yNi_{1-x-y}$ system, changes in the effective values of V_M and/or v are unlikely to be significant factors in causing the comparatively large variations of $N_{Al}^*(x, y)$ across the composition space (see Figure 12), and will not be discussed further.

4.8. Assessing $N_{Al}^*(x, y)$ on $Al_xFe_yNi_{1-x-y}$ CSAFs with the modified Wagner-Maak model

We have used the results shown in Figure 15 to consider possible physical insights into the complex dependence of $N_{Al}^*(x, y)$ on both composition and humidity that we have observed using $Al_xFe_yNi_{1-x-y}$ CSAFs. This was done by assuming that the oxidation of the CSAFs at 427 °C is diffusion-controlled, and can be accurately

described by the modified Wagner-Maak model given appropriate effective values of the kinetic parameters, as discussed earlier. In particular, Figure 15 was used to assess whether changes in values of the various parameters might explain the total range observed for N_{Al}^*, i.e. the difference between the maximum and minimum N_{Al}^* observed in the $Al_xFe_yNi_{1-x-y}$ system in either oxidizing environment. The highest value measured for N_{Al}^* in $Al_xFe_yNi_{1-x-y}$ was ~0.38, occurring at a composition of $Al_{0.38}Fe_{0.56}Ni_{0.06}$ in humid air, while the lowest measured value was ~0.15, occurring at $Al_{0.15}Fe_{0.74}Ni_{0.11}$ in dry air. Thus, the range of N_{Al}^* values was found to be 0.23. As illustrated in Figure 12, this minimum and maximum occur at a very similar Fe-to-Ni ratio in the two different environments, i.e. substituting ~10% H_2O by volume into dry air in a 427 °C oxidizing environment is apparently solely responsible for causing some change in the system that leads N_{Al}^* to increase by 0.23 in an $Al_xFe_yNi_{1-x-y}$ CSAF where $N_{Fe} / (N_{Fe} + N_{Ni}) \cong$ 0.90. If the modified Wagner-Maak model indeed applies to the system, then the addition of the small amount of humidity to the oxidizing environment must be resulting in a change in the effective values of one or more variables that cause a change in the critical Al concentration of $\Delta N_{Al}^* = 0.23$. Of the parameters analysed in Figure 15, only changes in D_{Al} or g^* are predicted to be individually capable of causing a $\Delta N_{Al}^* \geq 0.23$. This simple sensitivity analysis does not, of course, rigorously prove the importance of either parameter since the predicted N_{Al}^* depends on the values of all of the parameters which may be coupled to one another, and which might all change upon switching oxidizing environments. However, the analysis does reveal a vital aspect of the model: that the maximum possible value that can be predicted for N_{Al}^* is independent of the values of $N_O^{(s)}$, D_O, D_{Al}, and k_c. As noted earlier, these maximum N_{Al}^* solutions occur when Al enrichment is negligible and they depend only on g^*, V_M, and V_{ox}, as defined in Equation 19. Thus, for the highest measured value of N_{Al}^* ($Al_{0.38}Fe_{0.56}Ni_{0.06}$ in humid air) to be predicted by the modified Wagner-Maak model requires that $g^* \geq 0.54$, given the base values for V_M and V_{ox} shown in Table 1.

Before further considering the potential importance of the various parameters when applying the modified Wagner-Maak criterion to our $Al_xFe_yNi_{1-x-y}$ oxidation results at 427 °C, two important points must be made regarding the base values used for D_O and k_c in our sensitivity analysis. First, Stott [33] showed that the diffusion coefficient of

oxygen along the incoherent interface between Al_2O_3 and a bulk Ni lattice is orders of magnitude greater than that for diffusion through the lattice at temperatures between 800 and 1100 °C, and that this difference increases as temperature decreases. As a result, the effective value of D_O in the $Al_xFe_yNi_{1-x-y}$ CSAFs during oxidation at 427 °C is likely to be significantly higher at all compositions than the base value which was estimated by extrapolation of lattice diffusion data. Second, the base value of k_c was simply chosen to maximize the sensitivity of the predicted value of N_{Al}^* to small changes in k_c given the values already chosen for the other parameters. However, it is predicted from Equation 1 that, for this value of k_c, the total advancement depth, X, of the competitive scale (see Figure 13) will be only ~0.5 nm after 4 h oxidation time in an alloy where $N_{Al}^{(0)} < N_{Al}^*$. While determining precise values for X at different internally oxidized locations on the CSAFs was not practical given the characterization tools available to us, the XPS depth profiles taken in this region (e.g. Figure 7(i)) suggest that $X > 0.5$ nm, particularly at high Fe-to-Ni ratios where it appears that X may be on the order of tens of nm. Since k_c is a parabolic rate constant, this suggests that its actual value is likely several orders of magnitude higher than the base value across much of the composition space. As illustrated in Figure 15, higher effective values of D_O and k_c both tend to drive the modified Wagner-Maak model towards the physically limiting condition where Al enrichment is negligible. When this is the case, the N_{Al}^* predicted by the modified Wagner-Maak model is locally independent of all of the variables shown in Figure 15 except for g^*. If the model indeed applies to our system, then the $N_{Al}^*(x, y)$ boundary measured in dry air (Figure 12) would support the argument that oxidation of the $Al_xFe_yNi_{1-x-y}$ CSAFs at 427 °C occurs in a regime where Al enrichment is negligible. The reason for this is that we have previously shown that the total amount of competitive oxide that is formed increases significantly as the Fe-to-Ni ratio increases on the side of this boundary where $N_{Al}^{(0)} < N_{Al}^*$ (region 4) [23]. This indicates that the parabolic rate constant k_c must increase by orders of magnitude as the Fe-to-Ni ratio increases. Figure 15(d) shows that such an increase in k_c should generally favour an increase in N_{Al}^* but, in fact, the opposite trend is observed, i.e. the measured N_{Al}^* is significantly lower in AlFe than in AlNi, despite the much higher rate of competitive oxide growth.

This is consistent with a situation where no significant enrichment of Al is able to occur and, as a result, N_{Al}^* is essentially independent of k_c.

In terms of the modified Wagner-Maak criterion, it is highly likely that only system-dependent changes in the value of g^* could explain the wide range we have observed for N_{Al}^* in $Al_xFe_yNi_{1-x-y}$ exposed to dry or humid air at 427 °C. It appears to be physically unlikely that there can be any significant diffusive enrichment of Al during oxidation under these conditions, making the N_{Al}^* predicted by the model independent of all variables other than g^*, V_M, and V_{ox}. However, V_{ox} should remain constant and the dependence on V_M is weak, leaving g^* as the only variable in the modified Wagner-Maak model that might change to explain the large ΔN_{Al}^* observed upon varying the Fe-to-Ni ratio and/or the humidity of the oxidizing environment. Until recently, the value of g^* used in the Wagner or Wagner-Maak models has been widely assumed to be a constant, and in many cases has simply been taken as $g^* = 0.3$, a value determined experimentally by Rapp for oxidation of AgIn alloys at 550 °C [38]. Our results directly suggest that g^* may depend on both alloy composition and the oxidizing environment in $Al_xFe_yNi_{1-x-y}$ CSAFs at 427 °C, which could also be true in bulk alumina formers at higher temperatures. This is consistent with recent findings by Zhao et al., who studied the oxidation of bulk AlCrNi and AlNi samples at 1000 °C in dry air and 30% H_2O in air by volume [12,20]. They found that N_{Al}^* was higher in the humid environment and, by assessment using the unmodified Wagner-Maak criterion (described by Equations 17 and 18), concluded that only an increase in g^* due to the presence of the H_2O vapour could account for the ΔN_{Al}^* they observed. They also showed that internal Al_2O_3 precipitates formed in the humid environment were coarser and more widely spaced than those formed in the dry environment, and suggested that the difference in precipitate geometries might lead to different values of g^*. It is easy to rationalize that various factors that might depend on the specific precipitate geometry (e.g. the ratio of the Al_2O_3/M interface area to precipitate volume) could play an important role in determining the g^* at which oxygen diffusion will be blocked "sufficiently" for lateral Al_2O_3 growth to dominate.

If system-dependent variability of g^* is indeed significant, the ability to use the modified Wagner-Maak criterion to more accurately predict N_{Al}^* for generic AIM systems

would require a more advanced kinetic treatment of two major aspects of the model: (1) determining the value of g^* required for different systems based on the metal(s) represented by M and the geometry of the Al_2O_3 precipitates, and (2) determining the N_{AlO_v} that actually results from a given $N_{Al}^{(0)}$ when accounting for volume expansion effects. The first aspect was partially considered in another recent paper by Zhao et al., in which they show that, if specific precipitate-geometry effects are neglected, an expression for g^* can be derived which depends only on V_{ox} and V_M [39]. However, their equation was derived in the limit that $N_O^{(s)}D_O \ll N_{Al}^{(0)}D_{Al}$, and so is not likely to apply in systems where this is not the case, such as $Al_xFe_yNi_{1-x-y}$ at 427 °C. The second aspect is equally important because, even if an exact value of g^* could be determined, it must also be possible to predict the $N_{Al}^{(0)}$ required to obtain the N_{AlO_v} corresponding to that g^*. The simplifying assumptions used to develop both the unmodified and modified Wagner-Maak models neglect any effects of volume expansion due to diffusive Al enrichment or oxide formation and, as a result, are likely to limit the accuracy with which this can be done, particularly for large values of g^*. However, keeping this limitation in mind, Equation 19 can be used to calculate composition-dependent values of g^* from the $N_{Al}^*(x, y)$ boundaries that we have measured, since N_{Al}^* in $Al_xFe_yNi_{1-x-y}$ at 427 °C should be essentially independent of all other variables in the modified Wagner-Maak criterion, if it applies. Figure 16 shows the values of g^* calculated in this way as a function of Fe-to-Ni ratio for $Al_xFe_yNi_{1-x-y}$ oxidation in both the dry and humid air at 427 °C. Even if the internal oxidation of $Al_xFe_yNi_{1-x-y}$ at 427 °C cannot be accurately described by the Wagner-Maak model as shown in Figure 13 (i.e. is not diffusion-controlled), the concept of g^* is still likely to apply given the abrupt and marked transition we have observed between internal and external oxidation on the CSAFs. If this is the case, determining g^* values from N_{Al}^* using Equation 19 may still be generally appropriate, provided Al is not significantly enriched by some non-diffusive mechanism prior to Al_2O_3 precipitation. Even assuming Al enrichment is indeed negligible, the precise values of g^* shown in Figure 16 are unlikely to be accurate since Equation 19 does not account for volume expansion effects or details of the CSAF microstructure,

but the general trends observed in the dependence of g^* on the Fe-to-Ni ratio and oxidizing environment should be correctly representative of the system.

5. CONCLUSIONS

A high-throughput methodology was applied to the study of early oxidation of $Al_xFe_yNi_{1-x-y}$ CSAFs in humid air (~10% H_2O in air by volume) at 427 °C. A combination of characterization techniques was used to determine a continuous $N_{Al}^*(x, y)$ boundary between compositions that are passivated by formation of a surface or subsurface Al_2O_3 scale and those that are internally oxidized under these conditions. The work demonstrates the potential of CSAF-based high-throughput methods to rapidly screen complex oxidation responses across continuous regions of alloy composition space. Such approaches could prove particularly valuable in thoroughly vetting the effect of different oxidizing environments on alloy oxidation, as demonstrated by our comparison of the $N_{Al}^*(x, y)$ identified for $Al_xFe_yNi_{1-x-y}$ oxidation in humid air at 427 °C with that previously measured in dry air at the same temperature. While experimental constraints have limited the direct subject of our study to early oxidation of ternary thin films, the ability to create thicker CSAFs containing more components could, in principle, allow oxidation of alumina formers at much higher temperatures to be studied across any continuous plane of higher-order composition space. More importantly, the large amount of data generated by such high-throughput approaches could provide key fundamental insights into how to improve existing theoretical models in order to more accurately predict important properties like N_{Al}^*, which could aid in the development of improved alumina-forming alloys.

APPENDIX A

The XPS spectra used to construct the depth profiles were collected and analysed using *Thermo* Avantage (v4.88) software. The raw signals for the various oxidized and metallic species (before normalization by the sensitivity factors) were taken as the area of the peak or peaks assigned to each. Table A.1 shows the constraints used in the software to define the location and shape of each peak. Figure A.1 shows examples of resulting peak fits obtained using these constraints for spectra collected during the depth profiles. Examples of spectra containing metallic-only peaks (first row), metallic and oxidized peaks (second row), and oxidized-only peaks (third row) are provided for each Al 2s (first column), Fe $2p_{1/2}$ (second column), and Ni $2p_{3/2}$ (third column).

REFERENCES

[1]   F.H. Stott, G.C. Wood, J. Stringer, The Influence of Alloying Elements on the Development and Maintenance of Protective Scales, Oxid. Met. 44 (1995) 113–145.

[2]   R. Prescott, M.J. Graham, The Formation of Aluminum Oxide Scales on High-Temperature Alloys, Oxid. Met. 38 (1992) 233–254.

[3]   G. Wood, F. Stott, Oxidation of alloys, Mater. Sci. Technol. 3 (1986) 519–530.

[4]   Z.G. Zhang, F. Gesmundo, P.Y. Hou, Y. Niu, Criteria for the formation of protective Al2O3 scales on Fe–Al and Fe–Cr–Al alloys, Corros. Sci. 48 (2006) 741–765.

[5]   M.P. Brady, Y. Yamamoto, M.L. Santella, L.R. Walker, Composition, Microstructure, and Water Vapor Effects on Internal/External Oxidation of Alumina-Forming Austenitic Stainless Steels, Oxid. Met. 72 (2009) 311–333.

[6]   M.P. Brady, B. Gleeson, I.G. Wright, Alloy Design Strategies for Promoting Protective Oxide-Scale Formation, JOM. (2000).

[7]   B.A. Pint, J.R. DiStefano, I.G. Wright, Oxidation resistance: One barrier to moving beyond Ni-base superalloys, Mater. Sci. Eng. A. 415 (2006) 255–263.

[8]   D.J. Young, High Temperature Oxidation and Corrosion of Metals, Elsevier Science Limited, 2008.

[9]   R. Prescott, M.J. Graham, The oxidation of iron-aluminum alloys, Oxid. Met. 38 (1992) 73–87.

[10]   B. Chattopadhyay, G.C. Wood, The transient oxidation of alloys, Oxid. Met. 2 (1970) 373–399.

[11]   F.H. Stott, G.C. Wood, Internal Oxidation, Mater. Sci. Technol. 4 (1988) 1072–1077.

[12]   W. Zhao, B. Gleeson, Steam Effects on the Oxidation Behaviour of Al2O3-Scale Forming Ni-Based Alloys, Oxid. Met. 79 (2013) 613–625.

[13]   B.A. Pint, J. Leibowitz, J.H. DeVan, The Effect of an Oxide Dispersion on the Critical Al Content in Fe-Al Alloys, Oxid. Met. 51 (1999) 181–197.

[14]   J.H. DeVan, P.F. Tortorelli, The Oxidation-Sulfidation Behavior of Iron Alloys Containing 16-40 at% Aluminum, Corros. Sci. 35 (1993) 1065–1071.

[15]   J. Huang, H. Fang, X. Fu, F. Huang, H. Wan, Q. Zhang, S. Deng, J. Zu, High-Temperature Oxidation Behavior and Mechanism of a New Type of Wrought Ni – Fe – Cr – Al Superalloy up to 1300 ° C, Oxid. Met. 53 (2000) 273–287.

[16]   Y. Yamamoto, M.P. Brady, M.L. Santella, H. Bei, P.J. Maziasz, B.A. Pint, Overview of Strategies for High-Temperature Creep and Oxidation Resistance of Alumina-Forming Austenitic Stainless Steels, Metall. Mater. Trans. A. 42A (2011) 922–931.

[17]   M. Brady, Y. Yamamoto, M. Santella, P. Maziasz, B. Pint, C. Liu, Z. Lu, H. Bei, The Development of Alumina-Forming Austenitic Stainless Steels for High-Temperature Structural Use, JOM. (2008) 12–18.

[18]   M. Sakiyama, P. Tomaszewicz, G. Wallwork, Oxidation of iron-nickel aluminum alloys in oxygen at 600–800° C, Oxid. Met. 13 (1979).

[19]   J.R. Nicholls, P. Hancock, L.H. Al Yasiri, Optimising oxidation resistance of MCrAl coating systems using vapour phase alloy design, Mater. Sci. Technol. 5 (1989) 799–805.

[20]   W. Zhao, B. Gleeson, Assessment of the Detrimental Effects of Steam on Al2O3-Scale Establishment, Oxid. Met. 83 (2015) 607–627.

[21]   S.R.J. Saunders, M. Monteiro, F. Rizzo, The oxidation behaviour of metals and alloys at high temperatures in atmospheres containing water vapour: A review, Prog. Mater. Sci. 53 (2008) 775–837.

[22] N. Mu, K. Jung, N.M. Yanar, F.S. Pettit, G.R. Holcomb, B.H. Howard, G.H. Meier, The Effects of Water Vapor and Hydrogen on the High-Temperature Oxidation of Alloys, Oxid. Met. 79 (2013) 461–472.

[23] M.A. Payne, J.B. Miller, A.J. Gellman, High-throughput characterization of early oxidation across AlFeNi composition space, Corros. Sci. 91 (2015) 46–57.

[24] B. Fleutot, J.B. Miller, A.J. Gellman, Apparatus for deposition of composition spread alloy films: The rotatable shadow mask, J. Vac. Sci. Technol. A Vacuum, Surfaces, Film. 30 (2012) 061511: 1–10.

[25] G. Solferino, A.J. Anderson, Thermal reduction of molybdite and hematite in water and hydrogen peroxide-bearing solutions: Insights on redox conditions in Hydrothermal Diamond Anvil Cell (HDAC) experiments, Chem. Geol. 322-323 (2012) 215–222.

[26] S.S. Saleem, Infrared and Raman spectroscopic studies of the polymorphic forms of nickel, cobalt and ferric molybdates, Infrared Phys. 27 (1987) 309–315.

[27] C. Wagner, Reaktionstypen bei der Oxydation von Legierungen, Zeitschrift Für Elektrochemie. 63 (1959) 772.

[28] F. Maak, Untersuchungen über die Oxydation von Kupfer-Beryllium-Legierungen bei erhöhter Temperatur, Zeitschrift Für Met. 52 (1961) 545.

[29] F. Gesmundo, F. Viani, Transition from Internal to External Oxidation for Binary Alloys in the Presence of an Outer Scale, Oxid. Met. 25 (1986) 269–282.

[30] H.C. Yi, S.W. Guan, W.W. Smeltzer, A. Petric, Internal Oxidation of Ni-Al and Ni-Al-Si Alloys at the Dissociation Pressure of NiO, Acta Met. Mater. 42 (1994) 981–990.

[31] A.H. Heuer, D.B. Hovis, J.L. Smialek, B. Gleeson, Alumina Scale Formation: A New Perspective, J. Am. Ceram. Soc. 94 (2011) s146–s153.

[32] A.H. Heuer, T. Nakagawa, M.Z. Azar, D.B. Hovis, J.L. Smialek, B. Gleeson,

N.D.M. Hine, H. Guhl, H.-S. Lee, P. Tangney, W.M.C. Foulkes, M.W. Finnis, On the growth of Al2O3 scales, Acta Mater. 61 (2013) 6670–6683.

[33] F. Stott, G. Wood, D. Whittle, B. Bastow, Y. Shida, a Martinezvillafane, The transport of oxygen to the advancing internal oxide front during internal oxidation of nickel-base alloys at high temperature, Solid State Ionics. 12 (1984) 365–374.

[34] J.W. Park, C.J. Altstetter, The diffusion and solubility of oxygen in solid nickel, Metall. Trans. A. 18 (1987) 43–50.

[35] W. Gust, M. Hintz, a Lodding, H. Odelius, B. Predel, Impurity diffusion of Al in Ni single crystals studied by secondary ion mass spectrometry (SIMS), Phys. Status Solidi …. 187 (1981) 187–194.

[36] A. Green, N. Swindells, Measurement of interdiffusion coefficients in Co-Al and Ni-Al systems between 1000 and 1200°C, 1 (1985) 101–103.

[37] J.L. Meijering, Internal Oxidation in Alloys, in: H. Herman (Ed.), Adv. Mater. Res., John Wiley & Sons, Inc., 1971: pp. 1–81.

[38] R.A. Rapp, The transition from internal to external oxidation and the formation of interruption bands in silver-indium alloys, Acta Metall. 9 (1961) 730–741.

[39] W. Zhao, Y. Kang, J.M.A. Orozco, B. Gleeson, Quantitative Approach for Determining the Critical Volume Fraction for the Transition from Internal to External Oxidation, Oxid. Met. 83 (2014) 187–201.
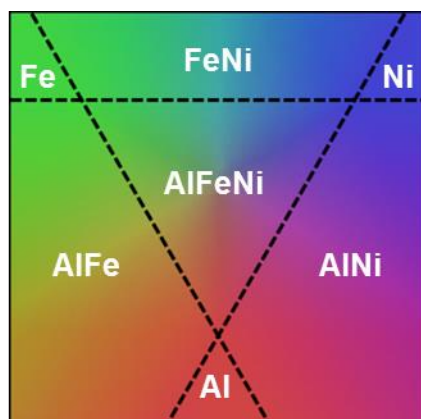
Figure 1. (Readers of the print article are referred to the digital version for colour figures.) Targeted spatial arrangement of an $Al_xFe_yNi_{1-x-y}$ composition distribution on a substrate surface to produce a full-range ternary CSAF. The central triangular region contains all possible ternary compositions and is surrounded by full-range binary and pure-component regions.
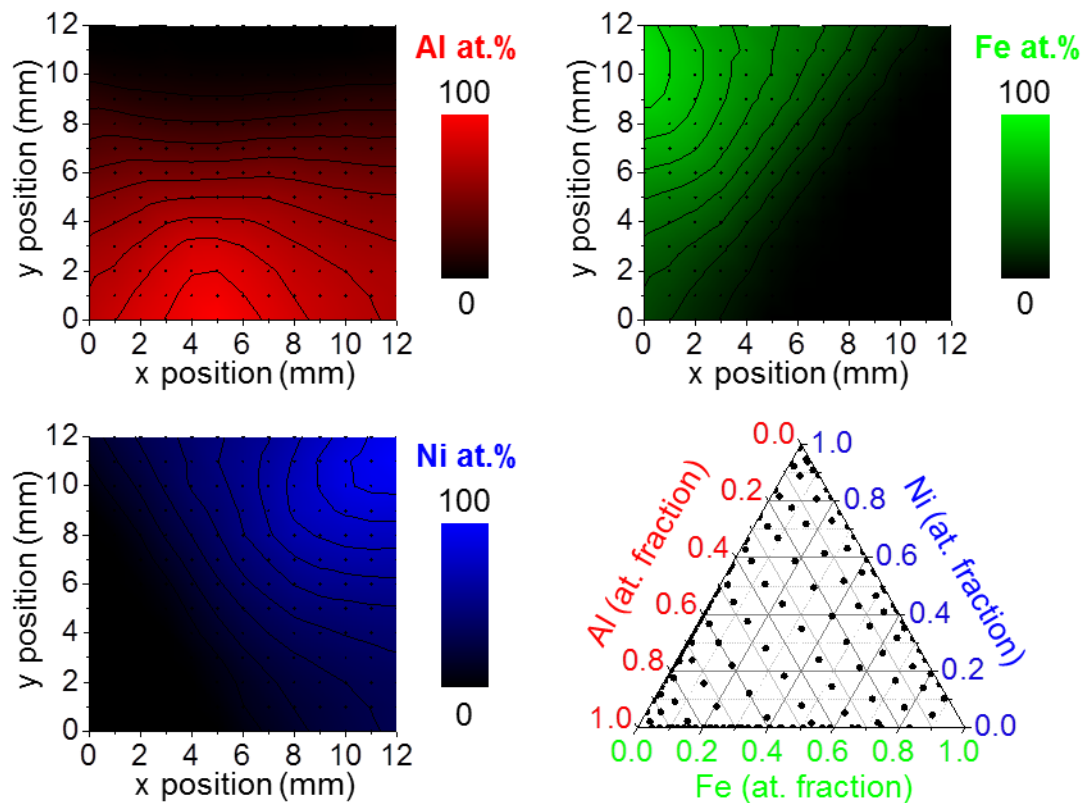
Figure 2. Real-space contour plots of the relative Al, Fe, and Ni concentrations in one of the CSAFs as determined by EDX measurements taken at the marked locations on a square grid. The set of discrete $Al_xFe_yNi_{1-x-y}$ compositions measured from the grid locations are plotted as points in the ternary composition diagram. Nearly complete coverage of $Al_xFe_yNi_{1-x-y}$ composition space is observed within the plotted region of the CSAF surface.
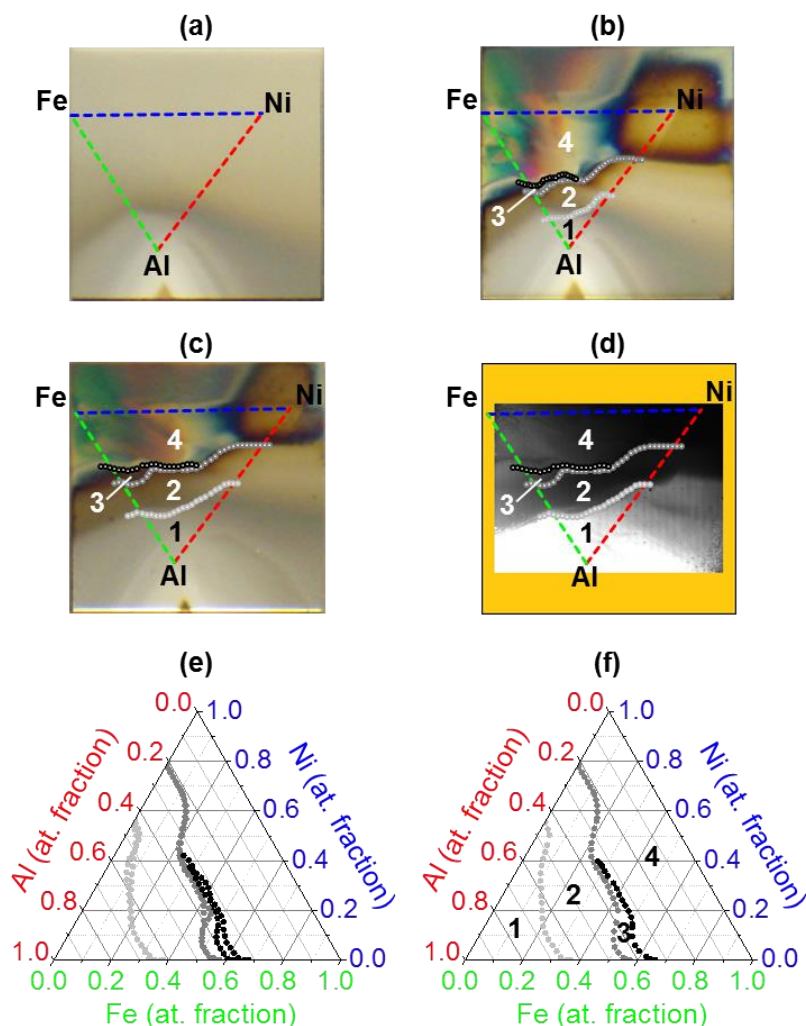
Figure 3. (Readers of the print article are referred to the digital version for colour figures.) **(a)** Photograph of one of the $Al_xFe_yNi_{1-x-y}$ CSAFs after deposition, UHV annealing (2 h at 427 °C), and brief (~15 min) exposure to ambient atmosphere. The location of the ternary-composition area as estimated by the CDM is shown for reference. **(b)** Photograph of the same CSAF after oxidation in humid air (10 mol% H_2O) for 4 h at 427 °C. The overlaid boundaries subdivide the surface into visually differentiable real-space regions 1-4. **(c)** Photograph of the second $Al_xFe_yNi_{1-x-y}$ CSAF used in the study after oxidation in humid air for 4 h at 427 °C. Boundaries are marked around regions that are qualitatively equivalent to those identified in (b). **(d)** Low-magnification SEM image of a large portion of the surface of the CSAF shown in (c). The transition from region 1 to region 2 appears clearly as an abrupt shift in contrast from light to dark. **(e)** Composition-space comparison of the boundaries identified in (b) and (c) after conversion by the respective CDM for each CSAF. **(f)** Average of the two sets of boundaries shown in (e).
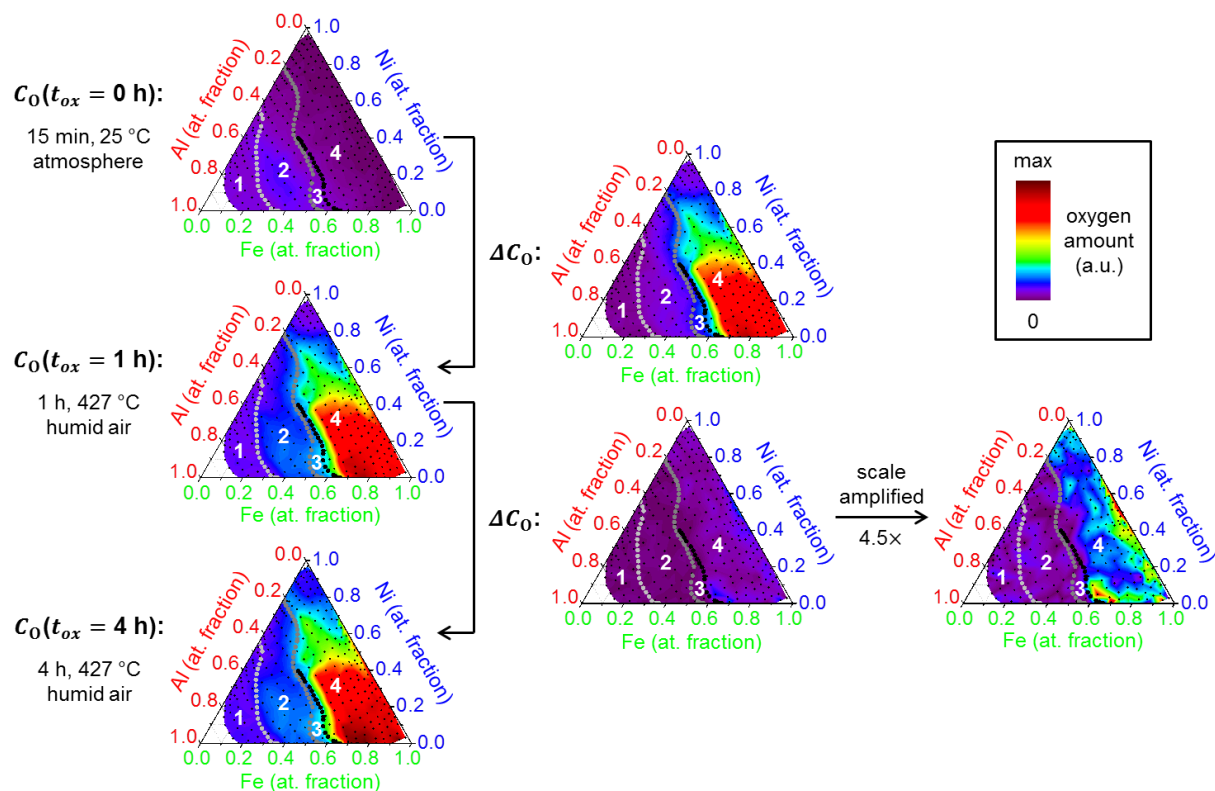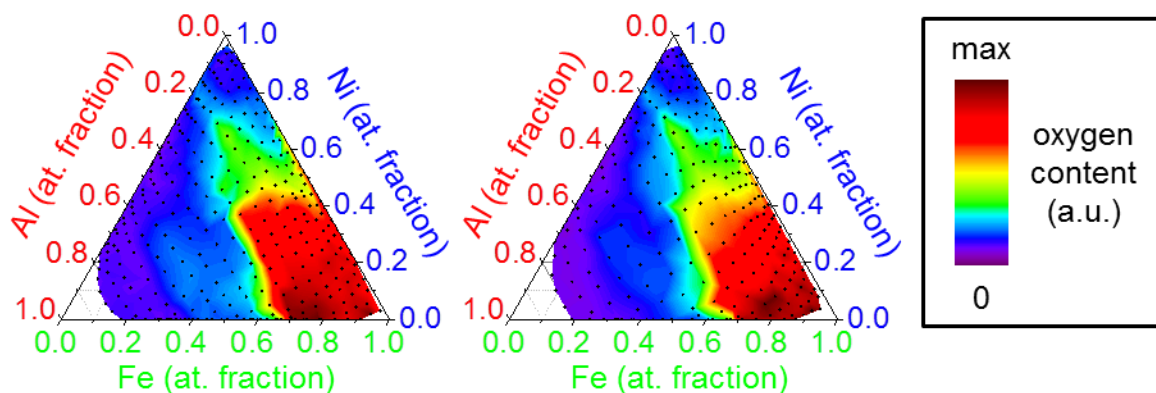
Figure 4. (Readers of the print article are referred to the digital version for colour figures.) EDX-measured oxygen content (C_O, left) and the change in oxygen content (ΔC_O, middle) plotted in composition space for one of the $Al_xFe_yNi_{1-x-y}$ CSAFs based on data collected after $t_{ox} = 0$, 1, and 4 h exposure to humid air (10 mol% H_2O) at 427 °C. The right-most composition map shows the ΔC_O data between 1 and 4 h replotted using an amplified (4.5×) scale. The regions identified by visual analysis are overlaid on each of the composition maps for reference. No significant uptake of additional oxygen is detectable in composition regions 1, 2, or 3 after the first hour.

Figure 5. (Readers of the print article are referred to the digital version for colour figures.) Composition-space comparison of EDX-measured oxygen content (C_O) in the two $Al_xFe_yNi_{1-x-y}$ CSAFs used in the study after exposure to humid air for 4 h at 427 °C. Although a different set of compositions was sampled in each case, the results are well reproduced between CSAFs.
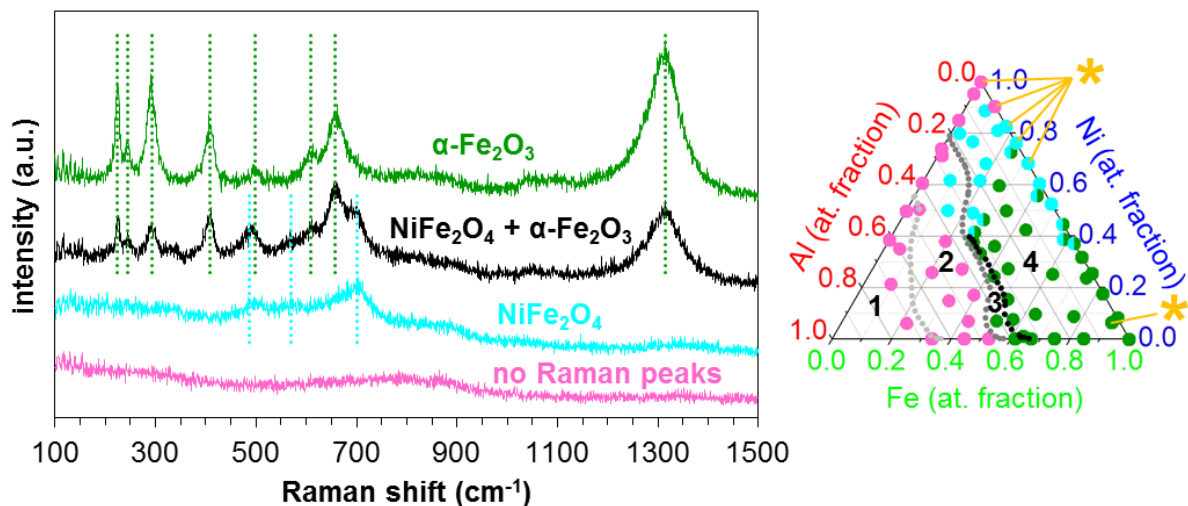
Figure 6. **Left:** Representative examples of the four primary types of Raman spectra observed at 69 locations across one of the $Al_xFe_yNi_{1-x-y}$ CSAFs after $t_{ox} = 4$ h in humid air at 427 °C. The spectra are offset and labelled with the oxide phases to which they are assigned. Characteristic peak locations are marked for $NiFe_2O_4$ at 486, 570, and 701 cm^{-1}; and for $\alpha\text{-}Fe_2O_3$ at 224, 245, 292, 409, 498, 609, 657, and 1315 cm^{-1}. **Right:** A ternary diagram showing the compositions of the $Al_xFe_yNi_{1-x-y}$ CSAF where the different types of spectra were observed. The boundaries identified by visual analysis are overlaid for reference. The $NiFe_2O_4$ + $\alpha\text{-}Fe_2O_3$ spectrum is indicated by a combination of $NiFe_2O_4$ and $\alpha\text{-}Fe_2O_3$ markers. The 6 spectra obtained at the compositions marked with an asterisk also contained weak, unassigned peaks, possibly attributable to trace Mo oxide phases having formed by interaction with the substrate.
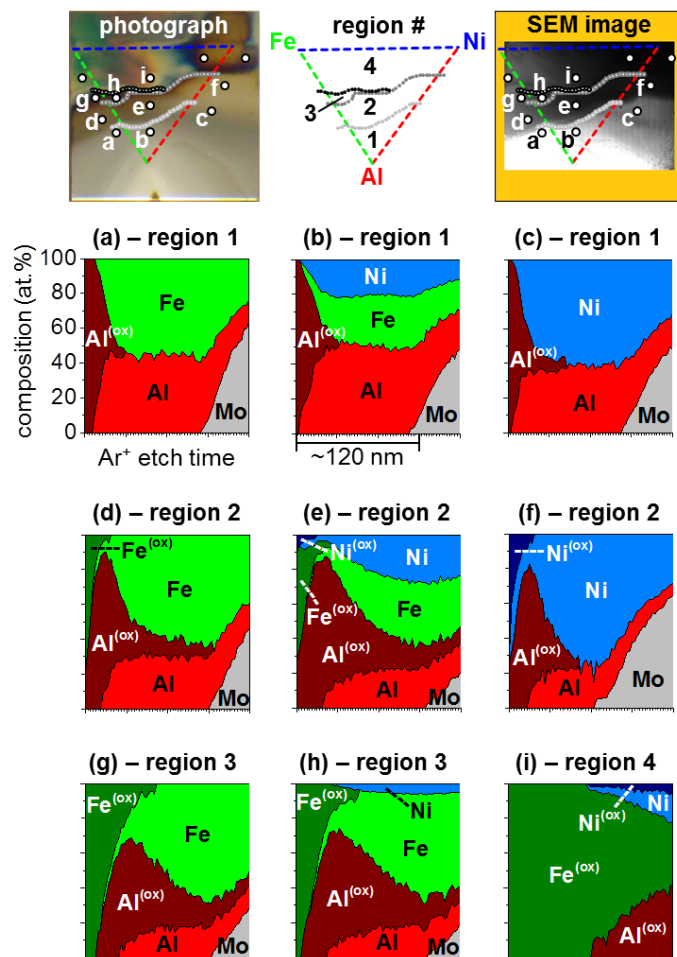
Figure 7. Top row: The 12 locations (white circles) at which XPS depth profiles were obtained shown on a photograph and an SEM image of an $Al_xFe_yNi_{1-x-y}$ CSAF (Mo substrate) after t_{ox} = 4 h in humid air at 427 °C. The triangular ternary-composition area with the regions identified by visual analysis is overlaid on each for reference. **(a)-(i)** The depth profiles obtained at the correspondingly labelled locations on the images. The plots show the relative atomic concentration of Al, Fe, Ni, and Mo in a metallic or oxidized state as determined from XPS spectra measured after each of the total Ar⁺ etch times marked by the hashes on the horizontal axes. Qualitatively similar profiles were obtained within each of the visually distinct regions 1-4. The extent of oxidation appears to increase with increasing region number.
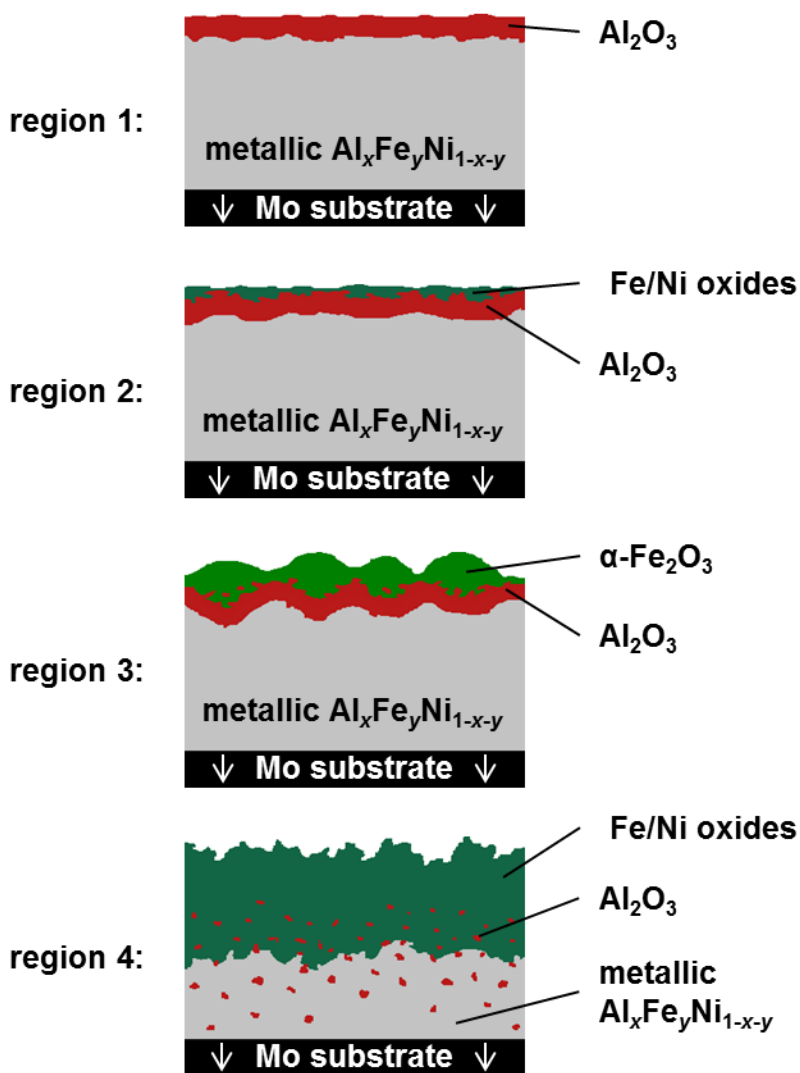
Figure 8. (Readers of the print article are referred to the digital version for colour figures.) Schematic depictions of the types of oxidation behaviour proposed for composition regions 1-4 of the $Al_xFe_yNi_{1-x-y}$ CSAFs exposed to humid air for 4 h at 427 °C. Based on the high-throughput spectroscopic analyses, a passivating Al_2O_3 scale appears to have formed at the surface of region 1, and in the subsurface of regions 2 and 3. Compositions in region 4 did not show evidence of Al_2O_3 passivation. Thus, the minimum initial Al content required for establishment of a passivating Al_2O_3 scale, $N_{Al}^*(x, y)$, is defined by the boundary of region 4.
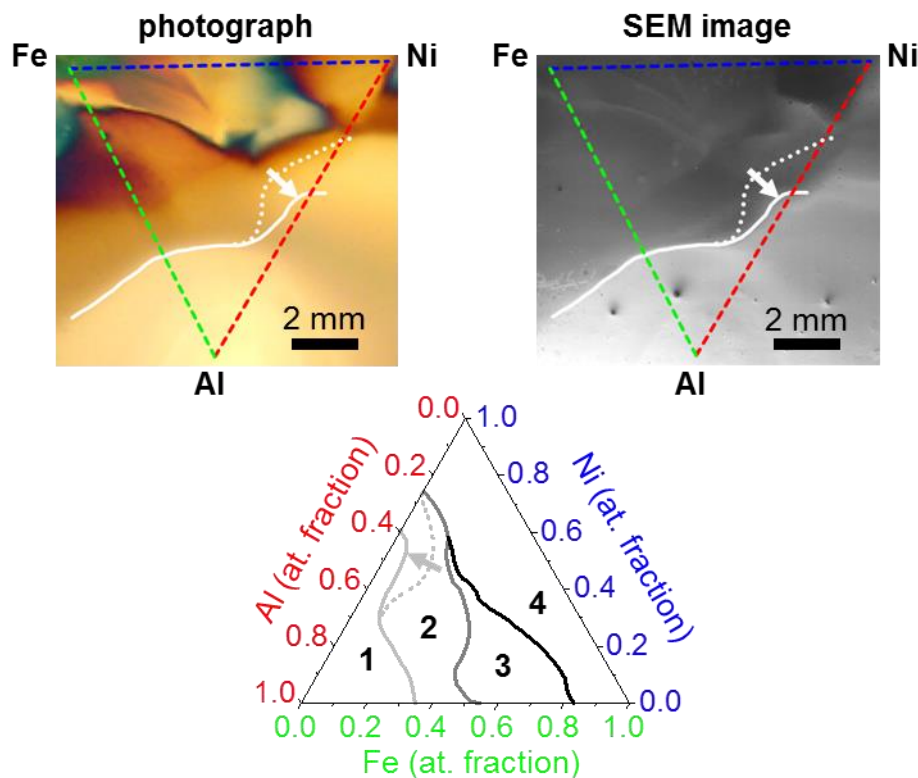
Figure 9. (Readers of the print article are referred to the digital version for colour figures.) **Top row:** A photograph and an SEM image of a portion of the surface of an $Al_xFe_yNi_{1-x-y}$ CSAF exposed to dry air for 4 h at 427 °C. The dotted line shows the trajectory of the boundary between regions 1 and 2 as determined by visual analysis of the photograph and reported in our previous study. The solid line shows the adjusted trajectory of the boundary based on SEM contrast, which has since been found to reveal the shift from region 1 to region 2 near the AlNi binary much more clearly than the visual image. **Bottom:** Adjusted map of the behaviour regions 1-4 for oxidation of $Al_xFe_yNi_{1-x-y}$ in dry air at 427 °C based on the reanalysis described above. Region 2 behaviour appears to extend to slightly higher Al contents at high Ni-to-Fe ratios than was initially reported. Otherwise, the map remains unchanged.
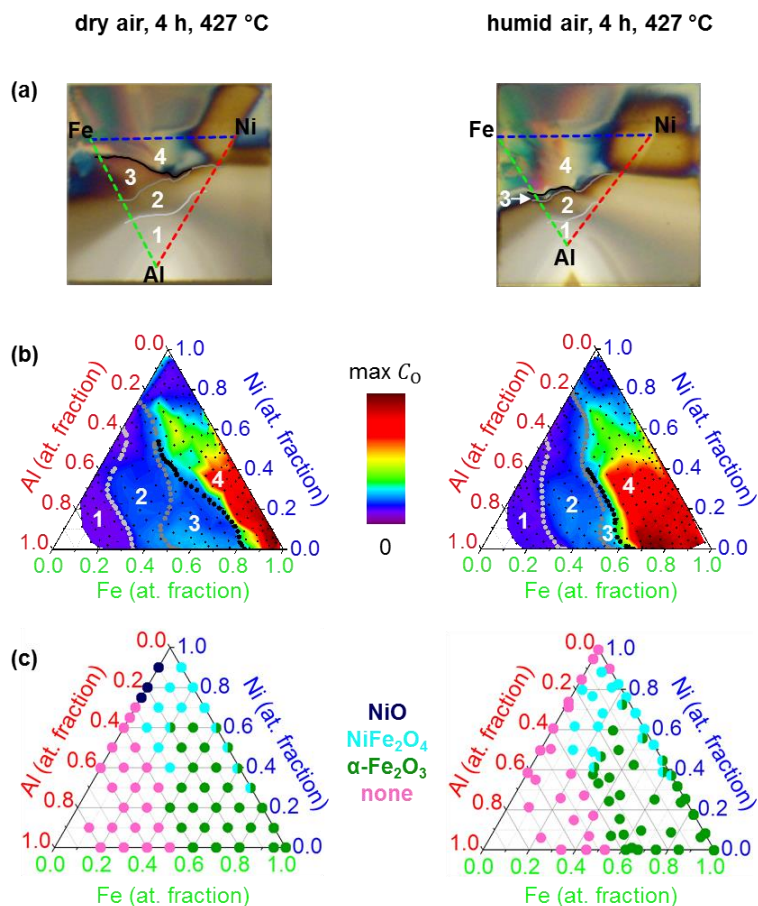
Figure 10. (Readers of the print article are referred to the digital version for colour figures.) A comparison of key results from the studies of $Al_xFe_yNi_{1-x-y}$ CSAFs oxidized in dry air (left) and humid air (right). **(a)** Photographs of the CSAFs after exposure to their respective environment for $t_{ox} = 4$ h. The ternary-composition areas and visually identified boundaries between composition regions 1-4 are overlaid for reference. **(b)** Composition maps of $C_O(t_{ox} = 4$ h$)$ in the two environments with the regions identified by visual analysis overlaid for reference. The high C_O values associated with region 4 extend across a notably larger fraction of composition space for oxidation in humid air. **(c)** Composition maps of the types oxide phases identified with Raman spectroscopy after $t_{ox} = 4$ h. The maps are very similar for the two different environments. The points on the humid-air map were chosen at real-space locations of interest on the CSAF surface and, thus, are not uniformly distributed in composition space.
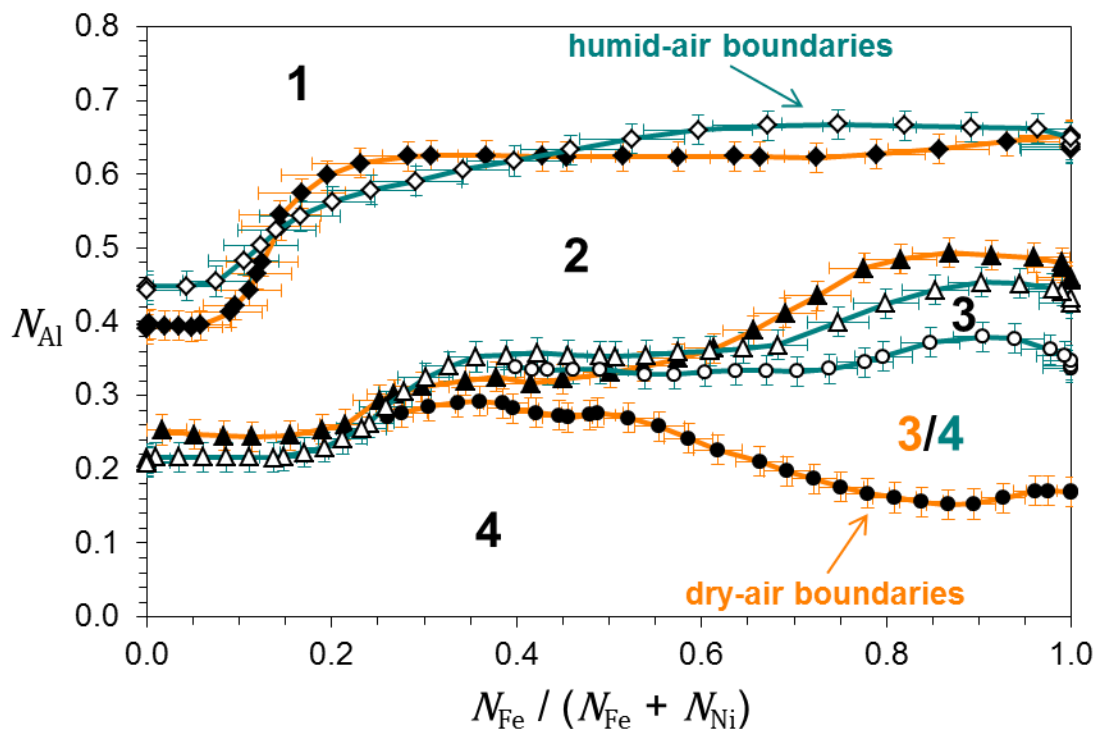
Figure 11. A comparison of the boundaries between composition regions exhibiting different types of oxidation behaviour determined by visual analysis of $Al_xFe_yNi_{1-x-y}$ CSAFs oxidized at 427 °C in either dry or humid air. The boundaries are plotted in composition space with Al atomic fraction as a function of the relative Fe atomic fraction compared to Ni. The error bars are representative of the experimental uncertainty of the visual analysis technique. The only measurably significant difference between the two environments is the shift of the boundary between regions 3 and 4 to higher N_{Al} values for humid air compared to dry air.
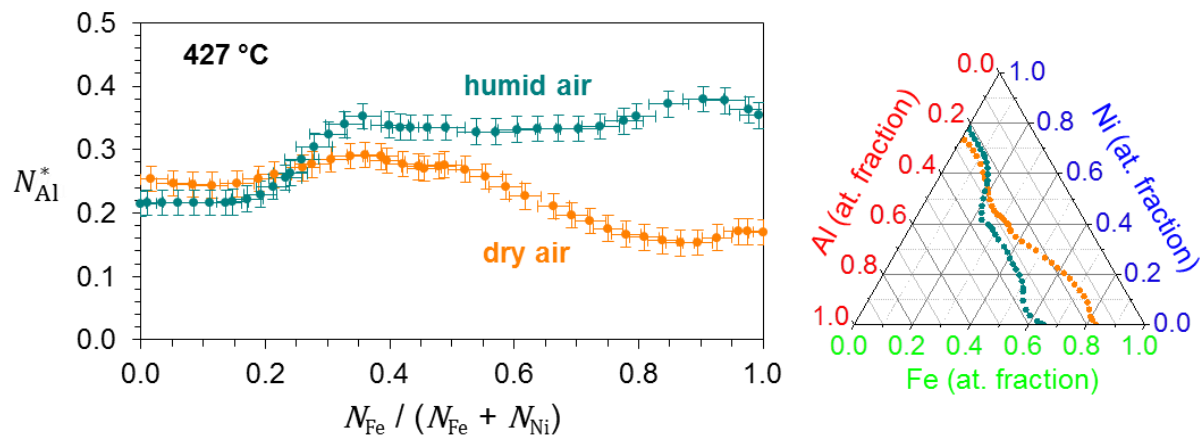
Figure 12. A comparison of $N_{Al}^*(x, y)$ in dry air and humid air at 427 °C as determined by high-throughput experimentation using $Al_xFe_yNi_{1-x-y}$ CSAFs. **Left:** The $N_{Al}^*(x, y)$ comparison in a rectangular representation of $Al_xFe_yNi_{1-x-y}$ composition space with Al atomic fraction as a function of the relative Fe atomic fraction compared to Ni. The error bars show the measurement uncertainty in the trajectory of the boundaries. **Right:** The $N_{Al}^*(x, y)$ comparison on a standard ternary composition diagram. Measurement uncertainty is not represented, but is shown in the plot at left.
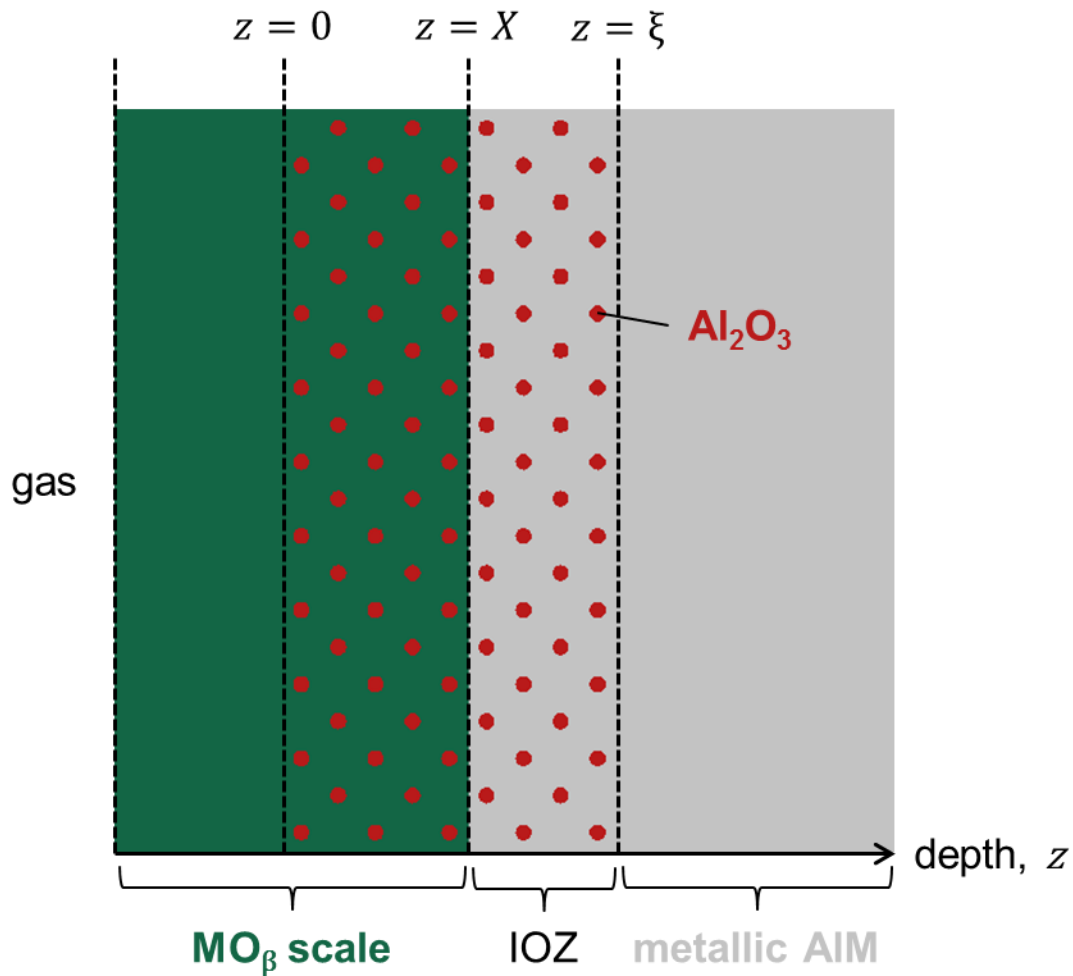
Figure 13. Schematic showing the cross section developed during internal oxidation of an AIM alloy according to the Wagner-Maak model. The original position of the interface between the alloy and gas is $z = 0$. The depth into the alloy bulk to which Al_2O_3 has been precipitated within the internal oxidation zone (IOZ) is $z = \xi$. The depth to which the IOZ has been subsequently overgrown by a competitive MO_β scale is $z = X$.
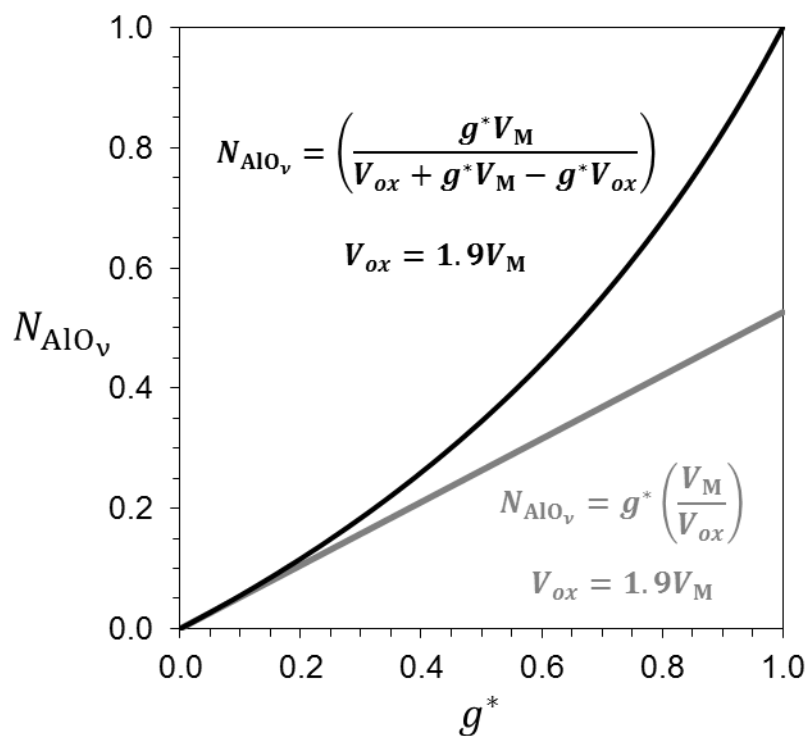
The plot displays:

$$N_{\mathrm{AlO}_v} = \left(\frac{g^*V_{\mathrm{M}}}{V_{ox} + g^*V_{\mathrm{M}} - g^*V_{ox}}\right)$$

$$V_{ox} = 1.9V_{\mathrm{M}}$$

$$N_{\mathrm{AlO}_v} = g^*\left(\frac{V_{\mathrm{M}}}{V_{ox}}\right)$$

$$V_{ox} = 1.9V_{\mathrm{M}}$$

Figure 14. Plot showing the N_{AlO_v} (mole fraction of AlO_v in an M/AlO_v mixture) corresponding to different values of g^* (the critical volume fraction of AlO_v in an M/AlO_v mixture) according to Equation 16 (grey) and Equation 19 (black) for a system in which $V_{ox} = 1.9V_{\mathrm{M}}$.
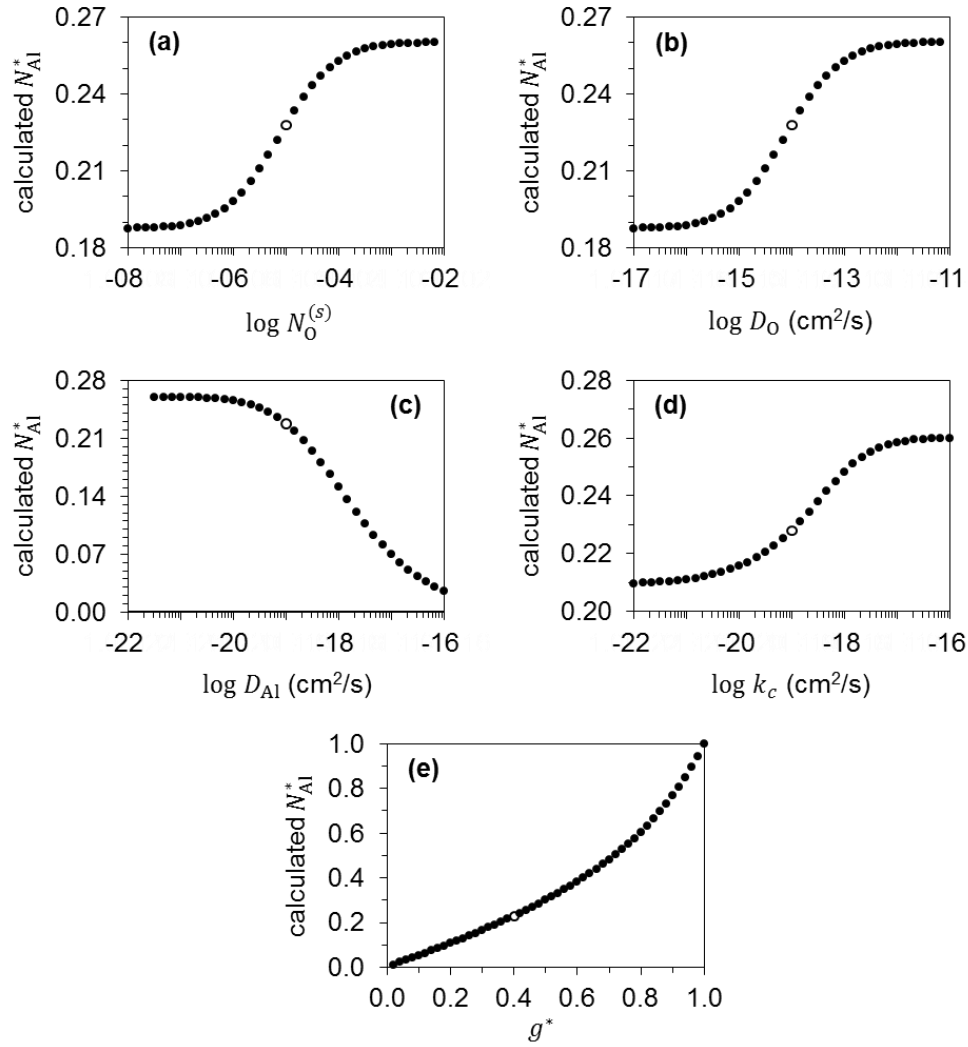
Figure 15. Plots showing the calculated value of N_{Al}^* for a range of values of different variables in the modified Wagner-Maak criterion with the others held at the base values shown in Table 1. The point shown as an open circle on each plot represents the solution when all the variables are set to the base values. **(a)** Semi-log plot showing the effect of changing the value of $N_O^{(s)}$. **(b)** Semi-log plot showing the effect of changing the value of D_O. **(c)** Semi-log plot showing the effect of changing the value of D_{Al}. **(d)** Semi-log plot showing the effect of changing the value of k_c. **(e)** Plot showing the effect of changing the value of g^*.
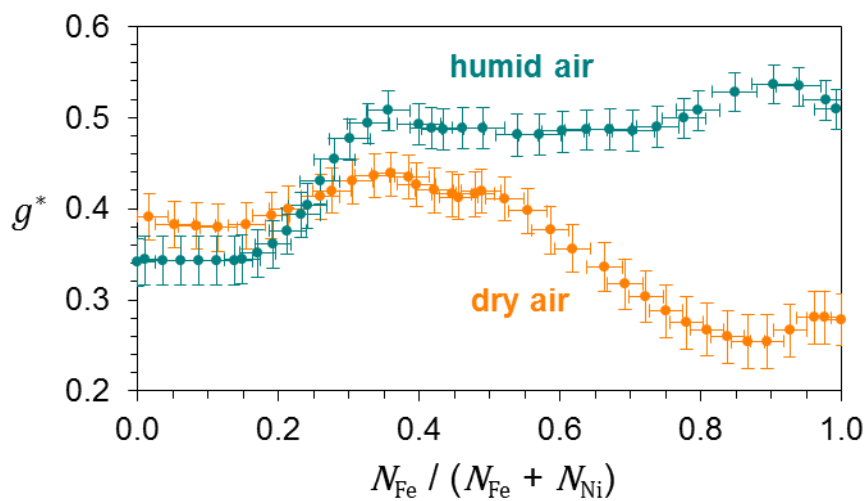
Figure 16. Plot showing the values of g^* corresponding to the measured $N_{Al}^*(x, y)$ boundaries for $Al_xFe_yNi_{1-x-y}$ oxidation in dry and humid air at 427 °C according to the modified Wagner-Maak criterion, assuming a limiting case where Al enrichment is negligible.
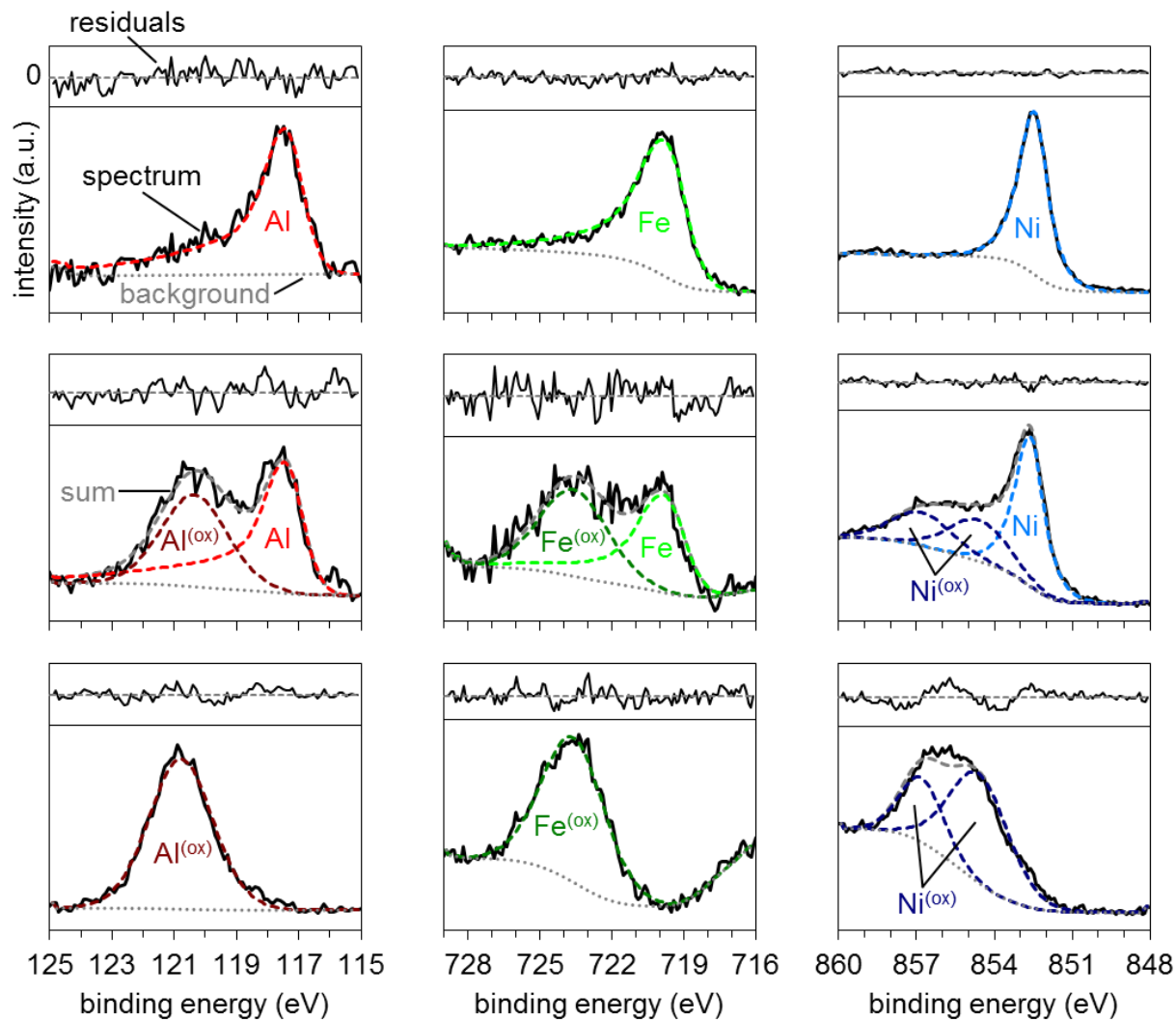
Figure A.1. The bottom sections of the plots show examples of the metallic/oxidized peak fitting for various Al 2s, Fe 2p$_{1/2}$, and Ni 2p$_{3/2}$ XPS spectra obtained during depth profiles of the Al$_x$Fe$_y$Ni$_{1-x-y}$ CSAF. Fitting of a *Thermo* "Smart" (modified Shirley) background was performed in each case and is included on the plots. The top section of each plot shows the residuals of the overall fit with the value of zero indicated by the horizontal dashed line.

TABLES

Table 1. Values used for sensitivity analysis of modified Wagner-Maak model

variable	base value	range	refs.
$N_O^{(s)}$	10^{-5}	$10^{-8} - 10^{-2}$	[33,34]
D_O	10^{-14} cm²/s	$10^{-17} - 10^{-11}$	[33,34]
D_{Al}	10^{-19} cm²/s	$10^{-22} - 10^{-16}$	[35,36]
k_c	10^{-19} cm²/s	$10^{-22} - 10^{-16}$	–
g^*	0.40	$0.00 - 1.00$	–
V_M	6.7 cm³/mol	n/a	–
V_{ox}	12.7 cm³/mol	n/a	–
ν	1.5	n/a	–

ACCEPTED MANUSCRIPT

Table A.1. Fitting constraints for XPS peaks used in *Thermo* Avantage software

peak	peak binding energy (eV)	FWHM (eV)	L/G mix product (%)	tail mix (%)	tail height (%)	tail exponent
Al	117.35-	1.36	30	50.50	0	0.0341
Al(ox)	117.45	2.4-2.6	30	100	0	0
Fe	119.0-121.0	2.00	30	30.00	0	0.0420
Fe(ox)	719.7-720.2	0.5-3.5	30	100	0	0
Ni	723.0-725.0	1.22	84	51.27	0	0.1411
Ni(ox)	852.4-853.4	2.80	30	100	0	0
(#1)	854.4-855.6	0.5-3.5	30	100	0	0
Ni(ox)	856.6-857.0	0.5-3.5	88	100	0	0
(#2)	393.7-394.0	0.5-3.5	30	100	0	0
Mo	397.0-398.5					
Mo(ox)						